A&A 646, A110 (2021)
https://doi.org/10.1051/0004-6361/202039218

Astronomy & Astrophysics

HOLISMOKES

III. Achromatic phase of strongly lensed Type Ia supernovae

S. Huber[1,2], S. H. Suyu[1,2,3], U. M. Noebauer[1,4], J. H. H. Chan[5], M. Kromer[6], S. A. Sim[7], D. Sluse[8], and S. Taubenberger[1]

[1] Max-Planck-Institut für Astrophysik, Karl-Schwarzschild Str. 1, 85741 Garching, Germany
e-mail: shuber@MPA-Garching.MPG.DE
[2] Physik-Department, Technische Universität München, James-Franck-Straße 1, 85748 Garching, Germany
[3] Institute of Astronomy and Astrophysics, Academia Sinica, 11F of ASMAB, No. 1, Section 4, Roosevelt Road, Taipei 10617, Taiwan
[4] Munich Re, IT1.6.4.1, Königinstraße 107, 80802 München, Germany
[5] Institute of Physics, Laboratory of Astrophysics, Ecole Polytechnique Fédérale de Lausanne (EPFL), Observatoire de Sauverny, 1290 Versoix, Switzerland
[6] Heidelberger Institut für Theoretische Studien, Schloss-Wolfsbrunnenweg 35, 69118 Heidelberg, Germany
[7] Astrophysics Research Centre, School of Mathematics and Physics, Queen's University Belfast, Belfast BT7 1NN, UK
[8] STAR Institute, Quartier Agora, Allée du Six Août, 19c, 4000 Liège, Belgium

Received 19 August 2020 / Accepted 7 December 2020

ABSTRACT

To use strongly lensed Type Ia supernovae (LSNe Ia) for cosmology, a time-delay measurement between the multiple supernova (SN) images is necessary. The sharp rise and decline of SN Ia light curves make them promising for measuring time delays, but microlensing can distort these light curves and therefore add large uncertainties to the measurements. An alternative approach is to use color curves where uncertainties due to microlensing are significantly reduced for a certain period of time known as the achromatic phase. In this work, we investigate in detail the achromatic phase, testing four different SN Ia models with various microlensing configurations. We find on average an achromatic phase of around three rest-frame weeks or longer for most color curves, but the spread in the duration of the achromatic phase (due to different microlensing maps and filter combinations) is quite large and an achromatic phase of just a few days is also possible. Furthermore, the achromatic phase is longer for smoother microlensing maps and lower macro-magnifications. From our investigations, we do not find a strong dependency on the SN model or on asymmetries in the SN ejecta. We find that six rest-frame LSST color curves exhibit features such as extreme points or turning points within the achromatic phase, which make them promising for time-delay measurements; however, only three of the color curves are independent. These curves contain combinations of rest-frame bands u, g, r, and i, and to observe them for typical LSN Ia redshifts, it would be ideal to cover (observer-frame) filters r, i, z, y, J, and H. If follow-up resources are restricted, we recommend r, i, and z as the bare minimum for using color curves and/or light curves since LSNe Ia are bright in these filters and observational uncertainties are lower than in the infrared regime. With additional resources, infrared observations in y, J, and H would be useful for obtaining color curves of SNe, especially at redshifts above ∼0.8 when they become critical.

Key words. gravitational lensing: micro – gravitational lensing: strong – supernovae: individual: Type Ia – cosmology: observations

1. Introduction

On the one hand, there is a tension in the Hubble constant H_0 of at least 4σ (Verde et al. 2019) between the early Universe measurements (Planck Collaboration I 2020) and late Universe measurements from the Cepheids distance ladder (e.g., Riess et al. 2016, 2018, 2019). On the other hand, the Hubble constant from the distance ladder using the tip of the red giant branch (Freedman et al. 2019, 2020) or surface brightness fluctuations for the calibration of Type Ia supernovae (SNe Ia, Khetan et al. 2020) is consistent with both the Planck results and the Cepheids. To assess this tension and whether new physics is required to reconcile it, independent methods and measurements of H_0 are important. Lensing time-delay cosmography is a powerful tool for measuring H_0 in a single step (Refsdal 1964), independent of other probes. The time delay can be inferred from a variable source, strongly lensed into multiple images by an intervening galaxy or galaxy cluster. This technique has been applied successfully to six lensed quasars to measure H_0 with 2.4% precision (e.g., Suyu et al. 2017; Courbin et al. 2018; Bonvin et al. 2018; Birrer et al. 2019; Sluse et al. 2019; Rusu et al. 2019; Chen et al. 2019; Wong et al. 2019), and more systems are being analyzed (Shajib et al. 2020; Millon et al. 2020; Birrer et al. 2020).

Instead of quasars, strongly lensed type Ia supernovae (LSNe Ia) are promising for measuring H_0 given that: (1) characteristic supernova (SN) light curve shapes make time-delay measurements possible on shorter time scales, (2) SNe fade away, facilitating measurements of the dynamics of the lens (Barnabè et al. 2011; Yıldırım et al. 2017, 2020; Shajib et al. 2018) to break model degeneracies, for example the mass-sheet degeneracy (Falco et al. 1985; Schneider & Sluse 2014), and (3) SNe Ia are standardizable candles that allow us to break model degeneracies, independently of dynamics, for lens systems whose lensing

magnifications are well characterized (Oguri & Kawano 2003; Foxley-Marrable et al. 2018). So far two LSNe with resolved multiple images have been observed, namely SN "Refsdal" (Kelly et al. 2016a,b) and iPTF16geu (Goobar et al. 2017), but we expect to find 500 to 900 LSNe Ia (Quimby et al. 2014; Goldstein & Nugent 2017; Goldstein et al. 2018; Wojtak et al. 2019) with the upcoming Rubin Observatory Legacy Survey of Space and Time (LSST).

To measure time delays between different images of a LSN Ia, one could use spectra, light curves and/or color curves. Problems arise from microlensing; this phenomenon is similar to strong lensing but instead of galaxies and galaxy clusters, the compact objects (for example, stars) located in the main lens also deflect the light. Due to the low masses of the microlenses, multiple images are typically not resolvable and for these cases microlensing is only observable as additional magnification. Originally predicted by Chang & Refsdal (1979), this phenomenon was unambiguously detected for the first time by Irwin et al. (1989) in the quasar QSO 2237+0305 as uncorrelated brightness variations between the four multiple images. More information on quasar microlensing is available in, for example, Schmidt & Wambsganss (2010) and Moustakas et al. (2019), and a general overview of microlensing is available in, for example, Wambsganss (2006) and Mediavilla et al. (2016). For our case, the additional magnification from stars in the lens galaxy influences images independently from one another and therefore adds uncertainties to the delay measurement (Yahalomi et al. 2017; Goldstein et al. 2018; Foxley-Marrable et al. 2018; Huber et al. 2019; Pierel & Rodney 2019).

While the influence of microlensing on spectra and light curves is strong in certain configurations, color curves have the following advantage: If microlensing affects light curves from different filters in a similar way, it cancels out in the color curves. This was first investigated by Goldstein et al. (2018), who show that microlensed color curves of LSNe Ia are "achromatic", in other words, their color curves are independent of microlensing for up to three rest-frame weeks after explosion, and therefore time-delay uncertainties are reduced from approximately 4% to 1% if color curves are used instead of light curves. Huber et al. (2019) investigated this further using the spherically symmetric W7 model (Nomoto et al. 1984; similar to Goldstein et al. 2018) for a specific magnification map (with lensing convergence $\kappa = 0.6$, shear $\gamma = 0.6$, and smooth matter fraction $s = 0.6$). Huber et al. (2019) also find the presence of an achromatic phase, but only for color curves where the specific intensity profiles are similar. In this paper, we explore the achromatic phase further, notably to test if it is only present in the W7 model or if other SN Ia models, including multidimensional and asymmetric ones, also show an achromatic phase. In addition, we investigate the dependency of the duration of the achromatic phase on different microlensing maps and color curves.

This paper is organized as follows. In Sect. 2, we present the different SN Ia models investigated in this work. The calculation of microlensed SN Ia light curves is shown in Sect. 3, and results are presented in Sect. 4. We conclude in Sect. 5.

2. SN Ia models and color curves

In Sect. 2.1 we give a short introduction to SNe Ia and the four theoretical models we use in this work. In Sect. 2.2 we compare the color curves from the theoretical models to an empirical model.

2.1. Theoretical SN Ia models

SNe Ia most likely have their origin in a thermonuclear explosion of a carbon-oxygen white dwarf (WD) (e.g., Hoyle & Fowler 1960), but details about the progenitor and explosion mechanism are still unknown. The classical textbook scenario is the single degenerate case where a non-rotating WD is stable until it approaches the Chandrasekhar mass limit, $M_{\rm Ch} \approx 1.4\,M_\odot$ (Whelan & Iben 1973; Nomoto 1982), due to the accretion from a main sequence star or a red giant. Today this classical scenario has lost some of its relevance and there are other mechanisms considered where the WD explodes before the Chandrasekhar mass is reached, which are typically called sub-Chandrasekhar (sub-Ch) explosions (Sim et al. 2010). Furthermore, for the thermonuclear burning, one distinguishes between detonation (supersonic shock) and deflagration (subsonic heat conduction). Another approach for SNe Ia is the violent merger mechanism that belongs to the family of double-degenerate scenarios in which the companion is another WD (see Pakmor et al. 2010, 2011, 2012, 2013). At the moment it is not clear which of the scenarios is the right one to describe SNe Ia and whether multiple scenarios or just a single one can explain the observed SN Ia explosions. More details can be found in, for example, Hillebrandt & Niemeyer (2000), Hillebrandt et al. (2013), and Livio & Mazzali (2018).

In this work we investigate four different SN Ia models to test the dependency of the achromatic phase on these models. The first one is the W7 model (Nomoto et al. 1984), a (parameterized) 1D deflagration of a carbon-oxygen white dwarf close to the Chandrasekhar mass ($M_{\rm Ch}$ CO WD) with 0.59 $M_\odot$ of ^{56}Ni, which is known to reproduce key observables of normal SNe Ia, for example, spectra (Jeffery et al. 1992; Nugent et al. 1997; Baron et al. 2006; Gall et al. 2012). Furthermore, we investigate the N100 model (Seitenzahl et al. 2013), which is a delayed detonation model, in other words, the burning starts as 3D deflagration and transitions into a detonation later, of a $M_{\rm Ch}$ CO WD. In this particular delayed detonation model, the explosion produced 0.6 $M_\odot$ of ^{56}Ni. The third model is a sub-Ch model with a carbon-oxygen WD of 1.06 $M_\odot$ producing 0.56 $M_\odot$ of ^{56}Ni (Sim et al. 2010). In addition, we consider a merger model from Pakmor et al. (2012) where two carbon-oxygen WDs of 0.9 $M_\odot$ and 1.1 $M_\odot$ collide and ignite a detonation in which 0.62 $M_\odot$ of ^{56}Ni are produced.

From our theoretical SN models we can get the observed flux $F_{\lambda,\rm o}(t)$ from which we can calculate AB magnitudes following

$$m_{{\rm AB},X}(t) = -2.5\log_{10}\left(\frac{\int {\rm d}\lambda\, \lambda S_X(\lambda)\, F_{\lambda,\rm o}(t)}{\int {\rm d}\lambda\, S_X(\lambda)\, c/\lambda} \times \frac{{\rm cm}^2}{\rm erg}\right) - 48.6 \quad (1)$$

(Bessell & Murphy 2012), where c is the speed of light and $S_X(\lambda)$ is the transmission function[1] for the LSST filter X (that can be u, g, r, i, z, or y), which are illustrated in Fig. 1.

2.2. Color curves of different SN Ia models

In this work we are especially interested in color curves and the dependence of the achromatic phase on the assumed theoretical SN Ia model. Therefore, we first compare in Fig. 2 the color curves of the SN Ia models used in this work to the empirical SN Ia model `SNEMO15` from Saunders et al. (2018) for six LSST color curves. We pick `SNEMO15` instead of `SNEMO2` or

[1] https://github.com/lsst/throughputs/tree/master/baseline

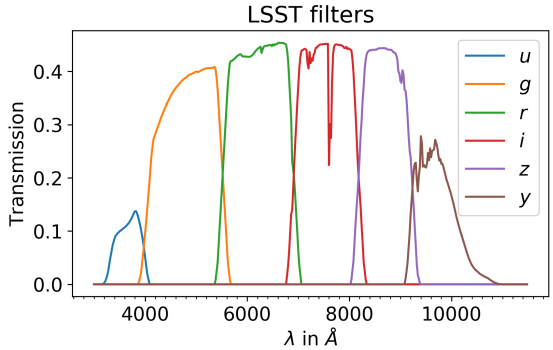

Fig. 1. Transmission for all six LSST filter bands. The effective wavelengths are $\lambda_{\rm eff}, u = 3671$ Å, $\lambda_{\rm eff}, g = 4827$ Å, $\lambda_{\rm eff}, r = 6223$ Å, $\lambda_{\rm eff}, i = 7546$ Å, $\lambda_{\rm eff}, z = 8691$ Å, and $\lambda_{\rm eff}, y = 9712$ Å.

SNEMO7 as this provides the largest variety in colors and therefore represents best the scatter of the colors based on real observations. To produce the median and 2σ (97.5th percentile−2.5th percentile) curves of SNEMO15, we consider all 171 SNe Ia from Saunders et al. (2018) used for training and validation of the empirical SN model. Furthermore, we use the flux from the empirical model to calculate the LSST color curves using Eq. (1). We note that the data cover only 3305 Å to 8586 Å, and therefore color curves containing the z and y bands cannot be calculated. Considering the u band, we find that the filter transmission becomes relevant around 3200 Å. Therefore, our presented u band light curve is an approximation, but a reasonably accurate one since flux drops further in the UV region at short wavelengths and the LSST filter transmission in the missing 100 Å region is low.

The comparison of the W7 model from this work to the one presented in Goldstein et al. (2018), where a different radiative transfer code has been used, shows a different trend in the color evolution. Details about uncertainties in the light curve shapes due to different ionization treatments in ARTIS can be found in Kromer & Sim (2009). A spectral comparison of different SN Ia models shows that differences are larger in early stages (∼8 days) in comparison to later epochs (∼30 days), but Suyu et al. (2020) point out as well that the exact spectral shapes depend on approximations that are used in the radiative transfer calculations (Dessart et al. 2014; Noebauer et al. 2017).

As we see in Fig. 2, none of the theoretical models are able to predict the color curves perfectly, but theses models are required to investigate impacts of microlensing on color curves and it is particularly interesting, how the microlensing signal differs between models. Furthermore, even though the values of the color curves for different models are offset, the overall color evolution do match the trend of SNEMO15. Although features are stronger in the theoretical models, they are still present in the color curves from SNEMO15. To measure time delays from color curves, features like extreme points or turning points would be crucial, to mitigate color differences between images due to differential dust extinction (Eliasdottir et al. 2006). Furthermore, these extreme or turning points should be located within the achromatic phase, to reduce uncertainties due to microlensing.

3. Microlensing on SNe Ia

The calculation of microlensing on SNe Ia, which we use in this work, is described in detail by Huber et al. (2019), who where motivated by the work of Goldstein et al. (2018). While both assumed the W7 model for the SNe Ia, Huber et al. (2019) calculated synthetic observables using the radiative transfer code ARTIS (Kromer & Sim 2009) whereas Goldstein et al. (2018) used SEDONA (Kasen et al. 2006). In the following, we briefly summarize the general idea.

To calculate microlensed light curves, we use the emitted specific intensity $I_{\lambda,\rm e}(t,p)$ at the source plane calculated via ARTIS for a given SN model, where $I_{\lambda,\rm e}(t,p)$ is a function of wavelength λ, time since explosion t, and impact parameter p, which is the projected distance from the ejecta center. We combine $I_{\lambda,\rm e}(t,p)$ with magnification maps from GERLUMPH (Vernardos et al. 2015; Chan, in prep.), which uses the inverse ray-shooting technique (e.g., Kayser et al. 1986; Wambsganss et al. 1992; Vernardos & Fluke 2013) yielding the magnification factor $\mu(x,y)$ as a function of cartesian coordinates x and y on the source plane[2].

Throughout this work, the specific intensity is treated in spherical symmetry and has therefore just a 1D spatial dependency on p. This approximation is exact for the W7 model and the sub-Ch model of Sim et al. (2010), and good for the N100 model, which produces nearly spherically symmetric ejecta, but results inferred from the asymmetric merger model are questionable. To estimate the impact of viewing angle effects we investigate the asymmetries in the merger model by using only photons from one half of the ejecta, for example, only averaging over photons that emerge in positive x-direction.

Magnification maps are determined by three main parameters, namely the convergence κ, the shear γ, and the smooth matter fraction $s = 1 - \kappa_*/\kappa$, where κ_* is the convergence of the stellar component. Furthermore, we assume a Salpeter initial mass function with a mean mass of the point mass microlenses of $\langle M \rangle = 0.35\,M_\odot$. Details of the initial mass function have negligible impact on our studies (Chan, in prep.). Our maps have a resolution of $20\,000 \times 20\,000$ pixels with a total size[3] of $10\,R_{\rm Ein} \times 10\,R_{\rm Ein}$. The Einstein Radius is a characteristic size of the map and can be calculated via

$$R_{\rm Ein} = \sqrt{\frac{4G\langle M\rangle}{c^2}\frac{D_{\rm s}D_{\rm ds}}{D_{\rm d}}}, \tag{2}$$

where $D_{\rm s}$, $D_{\rm d}$ and $D_{\rm ds}$ are the angular diameter distances from the observer to the source, from the observer to the lens (deflector), and between the lens and the source, respectively. To calculate these distances we assume a flat ΛCDM cosmology where we neglect the contribution of radiation ($H_0 = 72\,{\rm km\,s^{-1}\,Mpc^{-1}}$ and $\Omega_{\rm m} = 0.26$ as assumed by Oguri & Marshall 2010, hereafter OM10, our reference for typical LSN Ia images used in this work).

To calculate the observed microlensed flux we place the SNe Ia in the magnification map and solve:

$$F_{\lambda,\rm o}(t) = \frac{1}{{D_{\rm lum}}^2(1+z_{\rm s})}\int {\rm d}x \int {\rm d}y\, I_{\lambda,\rm e}(t,x,y)\,\mu(x,y), \tag{3}$$

where $D_{\rm lum}$ is the luminosity distance to the source. Furthermore, we interpolate the emitted specific intensity $I_{\lambda,\rm e}$ onto a 2D cartesian grid (x,y) with the same spatial resolution as the microlensing map and integrate over the whole size of the SN (Huber et al. 2019), which depends on the time after explosion. We then obtain the AB-magnitudes via Eq. (1).

[2] We note that μ denotes the magnification factor and not $\cos\theta$ as usually in radiative transfer equations.

[3] As a cross-check we investigated for a few cases larger maps with a total size of $20\,R_{\rm Ein} \times 20\,R_{\rm Ein}$, and our conclusions drawn in this work do not depend on the size of the maps.

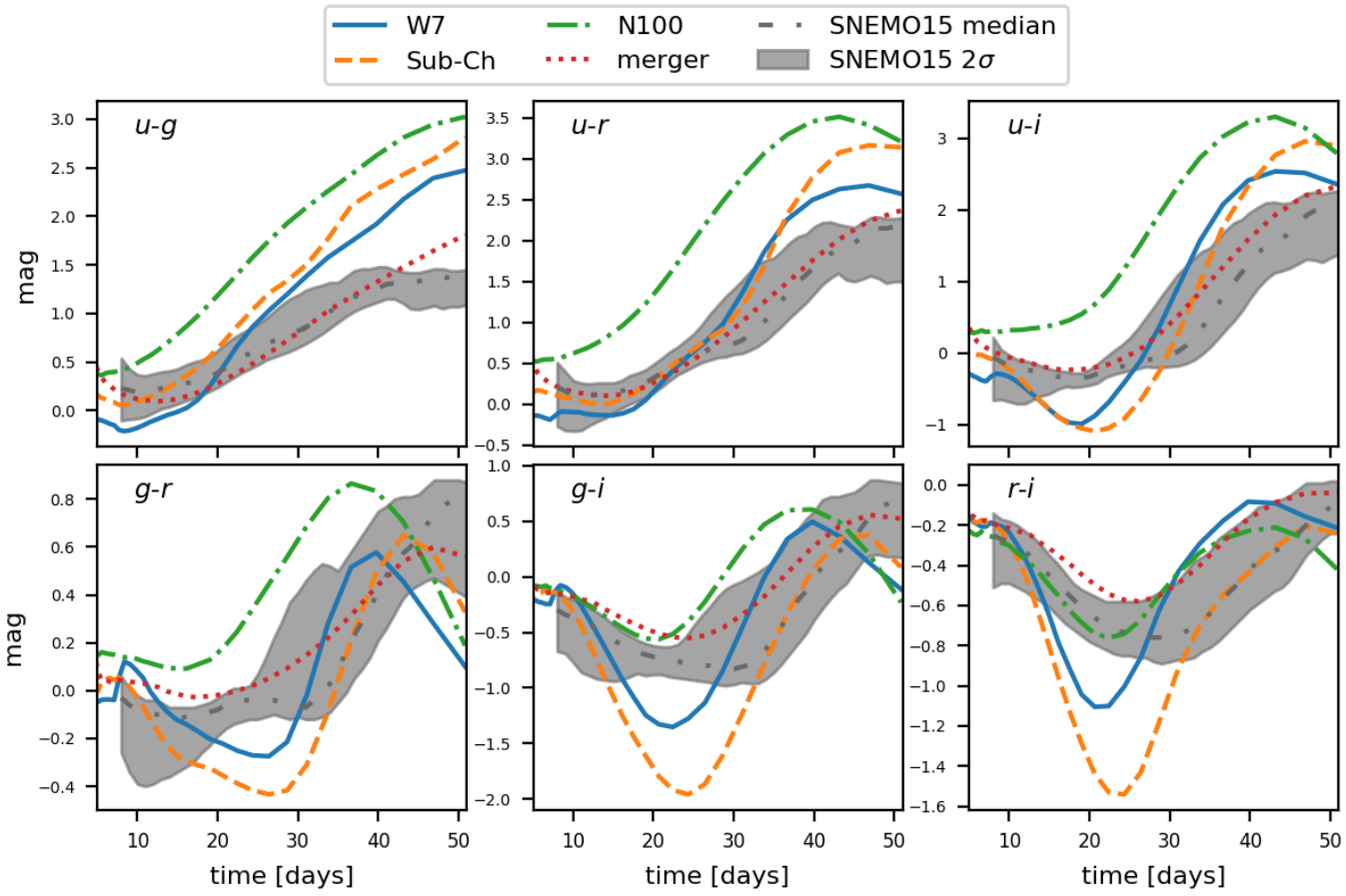

Fig. 2. Comparison of the four theoretical models: W7, N100, sub-Ch, and the merger to the empirical model `SNEMO15`.

Table 1. Summary of the number of different parameters investigated in Sects. 4.1–4.4.

Section	Models	Asymmetries	z_s, z_d	κ, γ	s	Color curves
4.1	4	No	1	6	5	15
4.2	4	No	4	2	5	15
4.3	1	6	1	2	5	15
4.4	4	No	3	2	5	15

Notes. In Sect. 4.1 the dependency on different models, smooth matter fractions and image configurations is investigated. Section 4.2 exhibits the dependency on the scale of the magnification map, Sect. 4.3 contains the investigations of asymmetries for the merger model, and Sect. 4.4 shows redshifted color curves.

4. Achromatic phase of LSNe Ia

In this section, we investigate the dependency of the achromatic phase on different parameters. Section 4.1 probes the four different SN Ia models (W7, N100, sub-Ch model, and the merger models) under the assumption of spherical symmetry. In addition, the dependency on the smooth matter fraction s and different image configurations (varying κ and γ) is discussed. Section 4.2 shows the dependency on the scale of the microlensing map defined via $R_{\rm Ein}$, which depends on the source and lens redshifts, z_s and z_d, respectively. In Sect. 4.3, effects of asymmetries in the merger model are investigated. While Sects. 4.1–4.3 assume rest-frame color curves, redshifted color curves are investigated in Sect. 4.4. In Table 1, we summarize the number of models and different magnification maps that are taken into account in the different sections.

4.1. SN Ia models, smooth matter fraction, and image configuration

To investigate the achromatic phase of LSNe Ia, we pick typical lens and image configurations from the OM10 catalog (Oguri & Marshall 2010). For the source and lens redshifts we assume $z_s = 0.77$ and $z_d = 0.32$, which are the median values of the OM10 catalog. We use redshifts in Sects. 4.1–4.3 only to calculate the scale of the microlensing maps, hence $R_{\rm Ein}$, and therefore the color curves discussed in these sections are in the rest-frame. The investigated κ and γ values are also based on OM10 and shown in Fig. 3 as six dark points for two different image types (minimum and saddle, in red and blue, respectively). For each of the two image types, the investigated points correspond to the median values and the 16th and 84th percentiles of the OM10 sample, taken separately for κ and γ. For each of the six pairs of κ and γ, five different s values (0.1, 0.3, 0.5, 0.7, and 0.9) are considered, which cover typical s values at image positions of galaxy-scale lenses (e.g., Schechter et al. 2014; Chen et al. 2018; Bonvin et al. 2019). Therefore, we have in total 30 magnification maps (from 6×5). Magnification maps for most configurations we investigate in this work are shown in Appendix A.

In comparison to the 30 different magnification maps probed in this work, Huber et al. (2019) have analyzed only a single magnification map ($\kappa, \gamma, s = 0.6$). Goldstein et al. (2018) investigated a much larger sample of LSNe Ia with 78 184

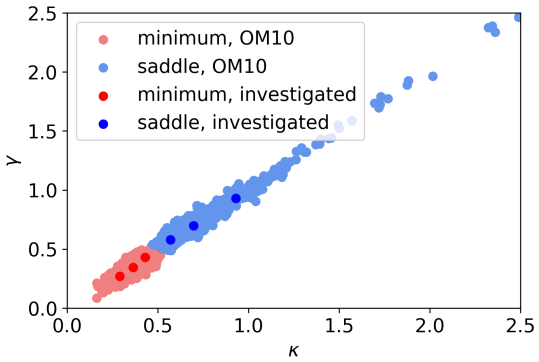

Fig. 3. Distribution of κ and γ values for two different image types (minimum and saddle, in red and blue, respectively), showing the sample of the OM10 catalog and the six pairs we have investigated $(\kappa, \gamma) = (0.29, 0.27), (0.36, 0.35), (0.43, 0.43), (0.57, 0.58), (0.70, 0.70)$, and $(0.93, 0.93)$). There are a few saddle points not shown in the plot going up to κ and γ values of around 10.

multiple images, but the sample is dominated by small-image-separation systems that will not be resolvable from ground-based monitoring, whereas we focus on spatially resolvable systems for cosmography by using the OM10 sample of strong lenses. Although our sample of LSNe Ia is much smaller, we probe per map 10 000 random positions instead of just one as by Goldstein et al. (2018); therefore, we investigate a much larger sample of microlensed SN Ia color curves, which further allows us to probe dependencies such as the duration of the achromatic phase on different image configurations.

In our analysis, we draw for each of the 30 magnification maps 10 000 random positions, where we calculate for each position all six LSST microlensed light curves following Eq. (1) and from these the 15 LSST color curves (obtained through all possible pair-wise combinations of the light curves). For each color curve, we consider the 1σ band ("full-width", corresponding to the difference between the 84th percentile and 16th percentile) and 2σ band (full-width, corresponding to the difference between the 97.5th percentile and 2.5th percentile) from the 10 000 random positions, which is shown in Fig. 4 for $g - i$ for $\kappa = 0.36$, $\gamma = 0.35$ and $s = 0.5$ for all 4 SN models investigated in this work. We use 32 time bins, covering rest-frame days 4.2 to 50.8 after explosion of the SNe Ia.

The black vertical lines in Fig. 4 correspond to the duration of the achromatic phase $t_{\rm achro}$ which we define as the first of two neighboring time bins where the 2σ band becomes larger than the threshold

$$\Delta_{\rm threshold} = \max(0.05\,{\rm mag}, \Delta_{3\%}), \quad (4)$$

where $\Delta_{3\%} = 0.03\,(\max({\rm color\,curve}) - \min({\rm color\,curve}))$. The reasoning behind these definitions is as follows. Typically the 2σ band increases with time but for rare cases it can exceed $\Delta_{\rm threshold}$ for a single time bin and then drop below that limit again. With our definition of $t_{\rm achro}$, including more than one time bin that exceeds $\Delta_{\rm threshold}$, we skip such outliers. If multiple time bins are within one day we require that all time bins exceed the $\Delta_{\rm threshold}$ in the 2σ band and set $t_{\rm achro}$ as the lowest time bin[4].

To motivate the 0.05 mag criterion, we look at a LSNe Ia at the median source redshift of OM10, $z_{\rm s} = 0.77$, and assume as an image the median minimum corresponding to $(\kappa, \gamma) = (0.36, 0.35)$ leading to a macro-magnification of 3.5. According to Huber et al. (2019), follow-up observations going between 1 and 2 mag deeper than LSST is ideal to measure time delays of LSNe Ia. Assuming observations of around 1.5 mag deeper than the LSST-like 5σ depth, we expect the 2σ uncertainties at the light curve peak of around 0.025 mag in r and i bands and higher uncertainties in other bands (LSST Science Collaboration 2009). This 2σ uncertainty corresponds to 0.05 mag in the 2σ band, and therefore our first limit in Eq. (4) assures that microlensing uncertainties within the achromatic phase are smaller than typical observational uncertainties. This is a very conservative estimate, especially for color curves having much larger changes than 0.05 mag over time. This motivates the use of $\Delta_{3\%}$ as the second criterion in Eq. (4). This means that for color curves covering more than ~1.7 mag over time the 0.05 mag criterion is replaced by the slightly larger value $\Delta_{3\%}$. Variations of color curves are always within 3 mag so uncertainties due to microlensing are kept within 0.09 mag in the achromatic phase.

As an illustration, the $g - i$ color curve in the upper-right-hand panel (sub-Ch) of Fig. 4 would have an achromatic phase of ~15 d with only the first criterion in Eq. (4), but an achromatic phase of ~35 d with both requirements, which is more appropriate given the large color variation. As a cross-check, we compared different definitions of the achromatic phase, namely, using only $\Delta_{\rm threshold} = 0.05$ or taking the mean of the first two time bins instead of requiring multiple neighboring bins. Although this changes the duration of the achromatic phase for some cases, our general conclusions from averaging over many different microlensing maps, color curves or models, are not influenced. While our definition of the achromatic phase is arbitrary to some extent, it is justified by looking at many plots as shown in Fig. 4, and we keep the definition consistent over the whole work, which allows us to compare different models and microlensing parameters.

In Fig. 4, we see that the duration of the achromatic phase for this example depends on the SN Ia model. While the model N100 has a short achromatic phase of ~15 d, the merger and sub-Ch models show a significantly longer duration of ~35 d and the W7 model is in between with ~25 d. This is related to the specific intensity profiles, shown in Fig. 5, for the radial distribution of the radiation in the six LSST filters. The influence of different specific intensity profiles on spectra and light curves is presented in detail in Appendix A of Huber et al. (2019).

The profiles for filters g and i for the sub-Ch model and N100 at day 14.9 show larger differences than W7 and the merger model, explaining the much shorter achromatic phase for the N100 model. The sub-Ch model reaches the 0.05 mag at a similar time as the N100 model but given the large range covered by the color evolution, the achromatic phase of the sub-Ch model is much longer. In the case of the merger model, the long achromatic time is explained by the intensity profiles because for later times (day 33.8), only the merger model still shows quite similar intensity profiles in g and i explaining the longer duration of the achromatic phase in the color curve $g - i$.

To draw a more general conclusion, we look at all color curves for the 6×5 magnification maps (see Table 1) for different SN Ia models as shown in Figs. 6 and C.1. For each of the 30 magnification maps, we have per color curve and model a $t_{\rm achro}$ from the 10 000 random positions as shown in Appendix B. The vertical lines in Figs. 6 and C.1 mark the mean values from the 30 $t_{\rm achro}$, and are matched in color and linestyles to that of the SN Ia models. In Fig. 6, six color curves are shown, which we refer to as useful color curves; these color curves have, for at least three SN models, substantially non-linear features like extreme points and turning points for delay measurements within their

[4] Only relevant for first few time bins since time is binned logarithmically.

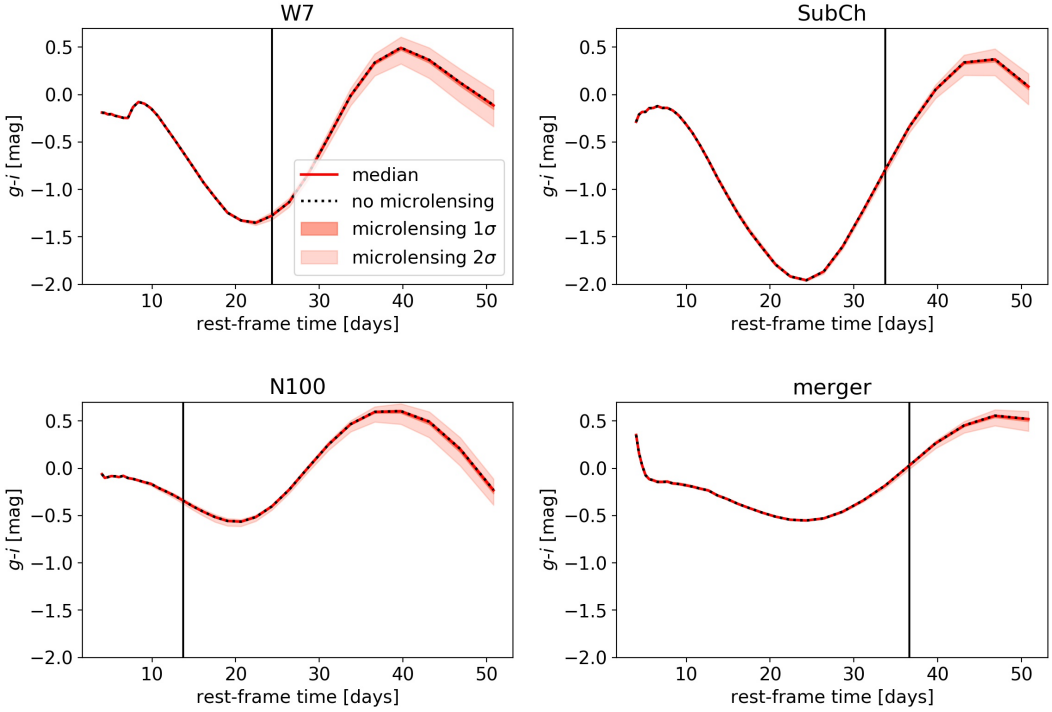

Fig. 4. Rest-frame LSST color curves for 10 000 random SN positions in the magnification map with $\kappa = 0.36$, $\gamma = 0.35$ and $s = 0.5$, comparing microlensed color curves (with median in solid red, and 1σ and 2σ band in different shades) to non-microlensed ones (dotted black). The vertical black lines indicate the duration of the achromatic phase. We find different durations of the achromatic phase for different SN Ia models, where the N100 model in this specific case has the shortest and the merger model the longest duration. This is just a specific case to illustrate the dependency of the achromatic phase on the specific intensity profiles. More general conclusions can be drawn from Figs. 6 and 7.

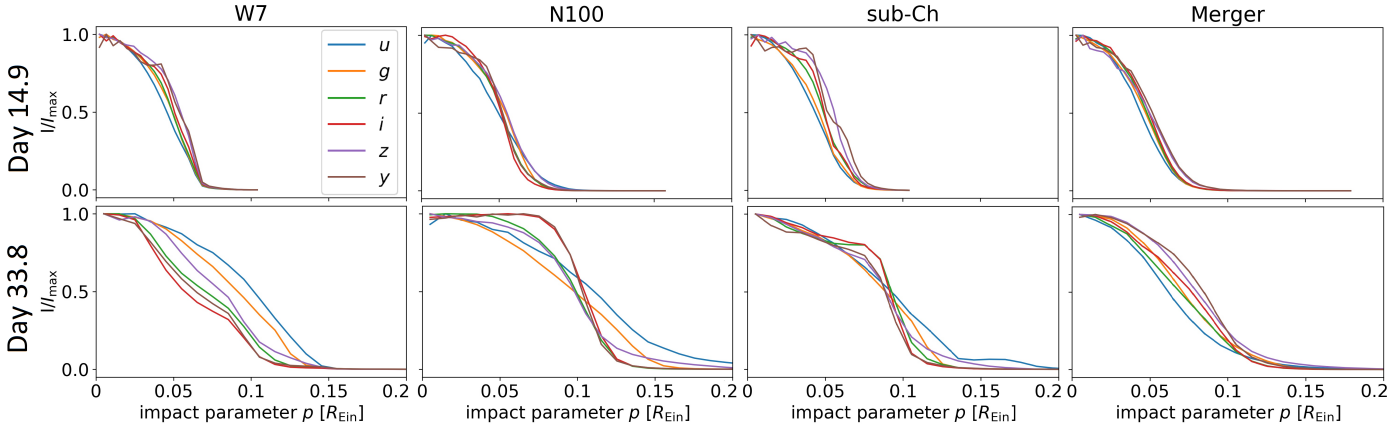

Fig. 5. Radial specific intensity profiles for four SN Ia models (W7, N100, the sub-Ch, and the merger model in the four labeled columns) for the six LSST filters at rest-frame day 14.9 (*top row*) and day 33.8 (*bottom row*) after explosion, where $R_{\rm Ein} = 2.9 \times 10^{16}$ cm for the median source and lens redshifts ($z_{\rm s}, z_{\rm d} = 0.77, 0.32$) based on OM10. Different SN Ia models yield different specific intensity profiles, leading to different durations of the achromatic phase. The wiggles for low p values at day 14.9 are most likely due to Monte Carlos noise and we do not expect them to be physical. For our microlensing calculations, differences at higher p values are more relevant, since events where micro caustics are crossed become more likely with larger radius.

corresponding achromatic phases. The remaining nine LSST color curves are shown in Fig. C.1. The most promising colors are rest-frame $u - i$, $g - r$, $g - i$, and $r - i$. The colors $u - g$ and $u - r$ are also encouraging but only if early features are captured. Therefore, to target the most promising color curves, rest-frame filters u, g, r, and i are necessary, which lead to three independent color curves. If one looks at the median color curves of the empirical SN model `SNEMO15` in Fig. 2, $g - r$ and $g - i$ are almost featureless within the achromatic phase in comparison to the theoretical SNe models. Nevertheless the message of the filters to target is not influenced since the other four promising color curves include filters g, r, and i anyway.

If one considers the median source redshift of the OM10 of $z_{\rm s} = 0.77$, the r band would be shifted from around 6200 Å to 11 000 Å and therefore mostly not observed in the LSST bands. This means that from the six promising color curves just rest-frame $u - g$ will be fully observed within the LSST bands. Assuming the nearby iPTF16geu system ($z_{\rm s} = 0.409$, Goobar et al. 2017), rest-frame $u - g$, $u - r$, and $g - r$ would be observed fully but colors containing rest-frame i band only

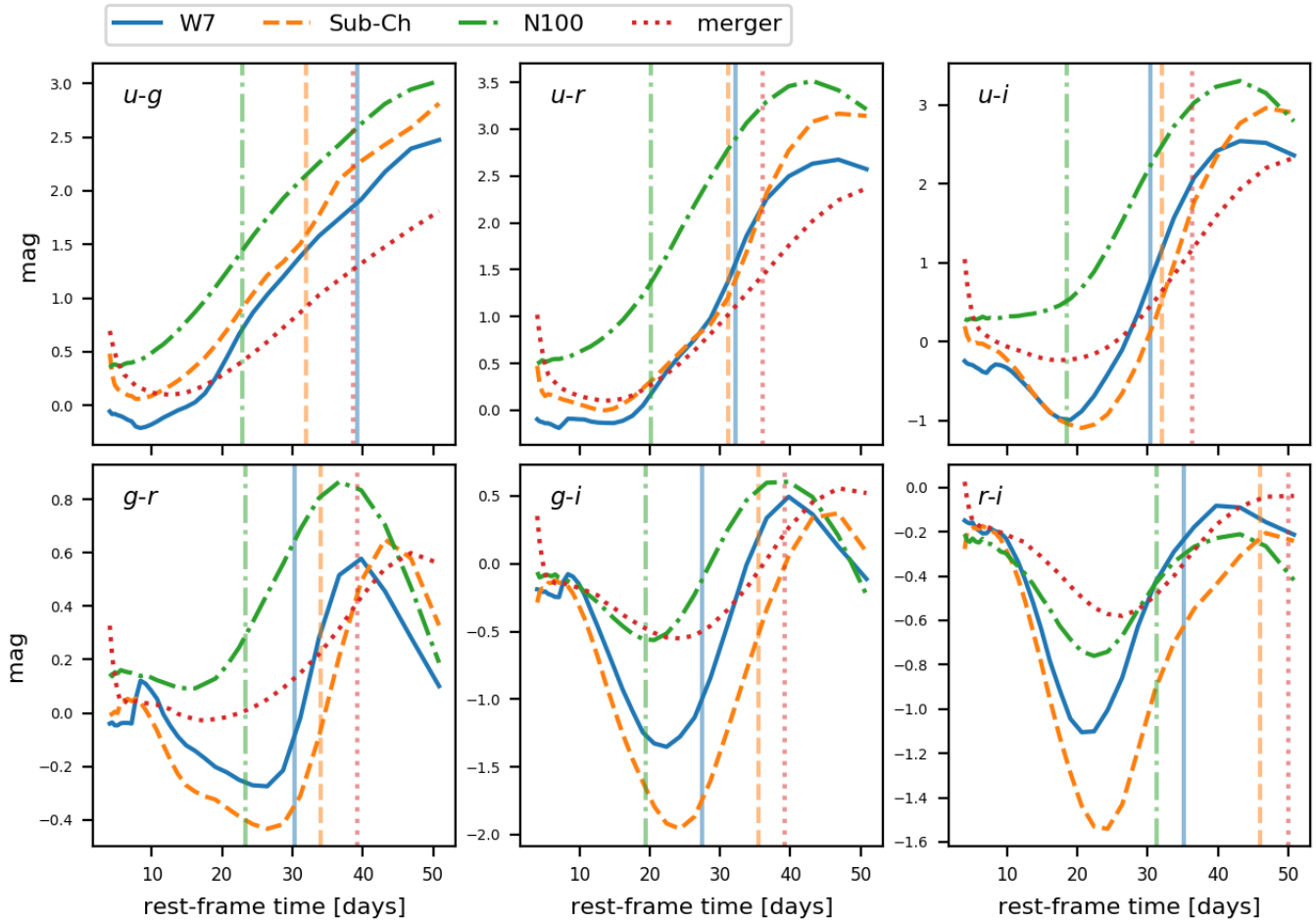

Fig. 6. Six rest-frame LSST color curves without microlensing for four different SN Ia models. The vertical lines mark the mean duration of the achromatic phase by averaging over 30 microlensing magnification maps (see Appendix B). This figure contains only the color curves that are promising for time-delay measurements (i.e., color curves exhibiting features like extreme points or turning points that are located within the achromatic phase for at least three SN Ia models). For the remaining nine LSST color curves see Fig. C.1.

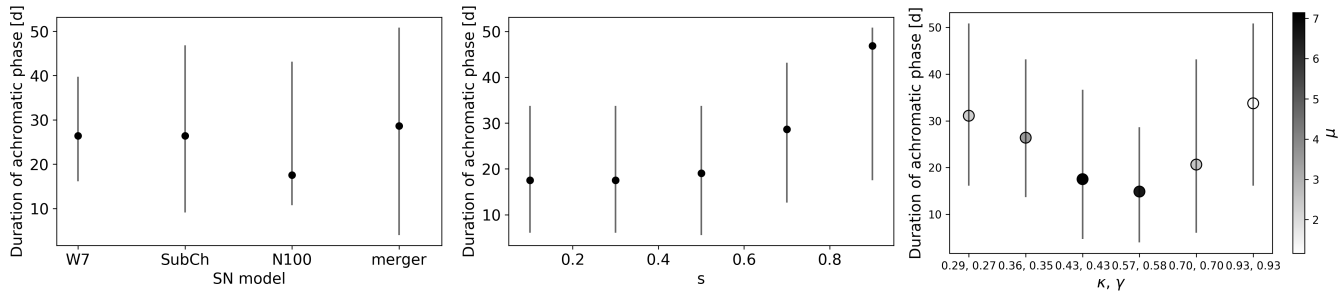

Fig. 7. Duration of the achromatic phase in rest-frame days for different SN Ia models (*left-hand panel*), different smooth matter fractions s (*middle panel*), and image configurations from strong lensing with their respective magnification factors μ shown in the color bar (*right-hand panel*). For these plots, a sample of four models, six different κ and γ values, five different s values, and 15 color curves has been investigated where we average over all parameters not shown on the x-axis. The dots correspond to the median, and the vertical bars indicate the range from the 16th to 84th percentiles. Due to limits in computing time, we only investigated the achromatic phase up to rest-frame day 50.8; therefore, for cases close to that limit, the presented result are a lower limit on the achromatic phase. While the median achromatic phase is typically $\gtrsim$20 rest-frame days, the spread due to different microlensing maps and color curves is quite large and the results can be seen in detail in Appendix B.

partly. This suggests that follow-up observations should also be conducted in the infrared, but the results show the problem that even though we find on average an achromatic phase of around three rest-frame weeks for nearly all colors, more than half of them might not be useful for time-delay measurements due to the lack of features in the color curves. A case where redshifted color curves are investigated is discussed in Sect. 4.4.

We emphasize that these results are based on averaging over the investigated sample of magnification maps. In special cases, the achromatic phase might be much shorter. The results are summarized in Fig. 7, where the median and the 16th to 84th percentiles of the achromatic-phase duration are shown. From the left-hand panel, we find that the SN Ia models W7, sub-Ch and the merger yield on average a comparable achromatic-phase

duration, and the N100 model has a shorter one. This might be related to the fact that the flux predicted by the N100 model around maximum light is too red in comparison to observations, which comes from an iron group element layer around a Ni-56 core (Sim et al. 2013), influencing the specific intensity profiles and therefore also the duration of the achromatic phase. However, given the uncertainties on the duration (shown in the left-hand panel) and our tests of different criteria for computing the achromatic-phase duration, we conclude that we do not find a significant dependency of the average achromatic phase on the SN model. In addition, we find from the right-hand panel that strong lensing images with a high macro-magnification $\mu = ((1-\kappa)^2 - \gamma^2)^{-1}$ are influenced more by microlensing than low magnification cases. Concerning the s value, we find similar durations of the achromatic phase for $s \leq 0.5$ and an increased duration if we go to smoother maps (middle panel). Depending on the position of the lensed images, an appropriate s value can be chosen (Barnabè et al. 2011; Oguri et al. 2014; Jiménez-Vicente et al. 2015). Overall we can say that combinations of κ, γ and s producing smoother microlensing maps yield a longer achromatic phase.

The spread of the 1σ range in Fig. 7 is large because there is quite some variation between different colors and microlensing maps, which makes it hard to give a general recipe for using color curves for time-delay measurements. Still, the median values in Fig. 7 are around three rest-frame weeks or longer and therefore follow-up resources for LSNe Ia should be allocated independent of the lensing parameters κ, γ and s.

4.2. Scale of magnification map

To probe the dependency on the scale of the microlensing map, namely $R_{\rm Ein}$, we investigated for $\kappa, \gamma = (0.36, 0.35)$ and $\kappa, \gamma = (0.70, 0.70)$ a range of redshifts, $(z_{\rm s}, z_{\rm d}) = \{(0.77, 0.32), (0.55, 0.16), (0.99, 0.48),$ and $(0.99, 0.16)\}$. The first pair corresponds to the median values from the OM10 and the second and third pair are the 16th and 84th percentile separately taken for $z_{\rm s}$ and $z_{\rm d}$. The fourth pair is the 84th percentile for $z_{\rm s}$ and 16th percentile of $z_{\rm d}$ to increase the variety of different $R_{\rm Ein}$. The results are summarized in Fig. 8. We find a very slight trend that with larger $R_{\rm Ein}$ the duration of the achromatic phase becomes longer. Given the large uncertainties, we cannot report this trend to be significant, even though it would be plausible because with larger $R_{\rm Ein}$ the physical size of the magnification maps increases, which causes SNe Ia to appear smaller in these maps, and for example events where micro caustics are crossed will be less likely. Nevertheless, Fig. 8 suggests that, if present at all, this effect is only minor.

4.3. Asymmetric merger model

In this section, viewing angle effects are investigated for the asymmetric merger model. We compare the spherically symmetric approach, which takes into account photon packets leaving the SN Ia ejecta in any direction and averages over them to get the 1D dependency on the impact parameter p, to six cases where only photons from one half of the ejecta are taken into account, for example, just photons that leave the ejecta at a positive x-coordinate, which we label as $x > 0$. For this subset we also calculate the 1D impact parameter, but just averaging over photons leaving the ejecta at $x > 0$. The other cases that we investigate are $x < 0$, $y > 0$, $y < 0$, $z > 0$, and $z < 0$, and the results are shown in Fig. 9. We find that viewing angle effects influence shapes of color curves and also the duration of the achromatic phase, but only slightly and therefore useful color curves (marked by red frames) are the same as those pointed out in Sect. 4.1.

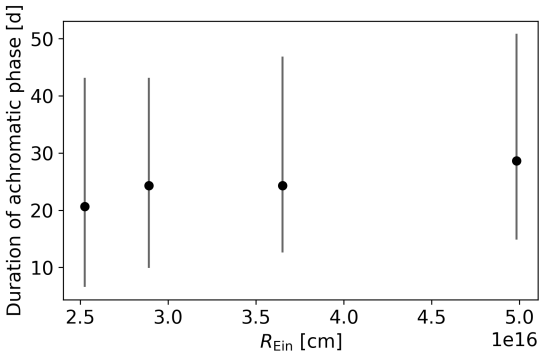

Fig. 8. Duration of achromatic phase as a function of $R_{\rm Ein}$, the scale of variations in the microlensing map. The dots correspond to the median and the vertical bars indicate the range from the 16th to 84th percentile for the sample of four models, two different κ and γ pairs, five different s values, and 15 color curves that have been investigated, where we average over all parameters not shown on the x-axis. From left to right, $R_{\rm Ein}$ corresponds to $(z_{\rm s}, z_{\rm d}) = (0.99, 0.48), (0.77, 0.32), (0.55, 0.16), (0.99, 0.16)$.

4.4. Redshifted color curves

Section 4.1 indicates that most useful color curves (curves with features for measuring time delays within the achromatic phase) in the SN rest-frame will be shifted to the infrared regime for typical redshifts expected for LSNe Ia. This section investigates if useful color curves can still be found in *ugrizy* coming from the rest-frame ultraviolet (UV), taking into account typical redshifts of SNe Ia. For this, we consider a set of representative redshifts: $z_{\rm s}, z_{\rm d} = \{(0.55, 0.16), (0.77, 0.32),$ and $(0.99, 0.48)\}$.

The results for $z_{\rm s} = 0.55$ are shown in Fig. 10. In comparison to the rest-frame bands, we see from Fig. 1 that the u band will be observed in r, the g band in i, the r band in y, and the rest will be in the infrared regime not covered by LSST filters. Accordingly, we find three useful rest-frame color curves from Figs. 6–10, namely $u-g$ is redshifted roughly to $r-i$, $u-r$ to $r-y$, and $g-r$ to $i-y$, although only two of the color curves are independent. Unfortunately none of the color curves coming from the rest-frame UV show strong features within the achromatic phase in at least three models that would be promising for time-delay measurements. The cases for $z_{\rm s} = 0.77$ and $z_{\rm s} = 0.99$ are presented in Appendix C. For $z_{\rm s} = 0.77$ we find two useful independent color curves for time-delay measurement, namely $i-z$ and $z-y$, but at $z_{\rm s} = 0.99$ there is only $z-y$ remaining in the observed u through y bands. For some color curves like $g-i$ for $z_{\rm s} = 0.55$ or $r-z$ for $z_{\rm s} = 0.77$ one might argue that they are also useful if early features are captured but this is because they still contain a substantial amount of rest-frame $u-g$. Nevertheless we see the trend that with higher redshifts useful color curves are shifted to bands covering higher wavelengths but there are no useful color curves coming from the rest-frame UV. Therefore, the number of useful color curves observed in u through y bands decreases with higher redshift. As discussed by Suyu et al. (2020), the exact spectral shapes particularly of the rest-frame UV spectra depend on various approximations used in the radiative transfer calculations, such as metallicity of the progenitor or the number of ionization states (e.g., Lucy 1999; Lentz et al. 2000; Kromer & Sim 2009; Walker et al. 2012; Dessart et al. 2014; Kromer et al. 2016; Noebauer et al. 2017), and therefore

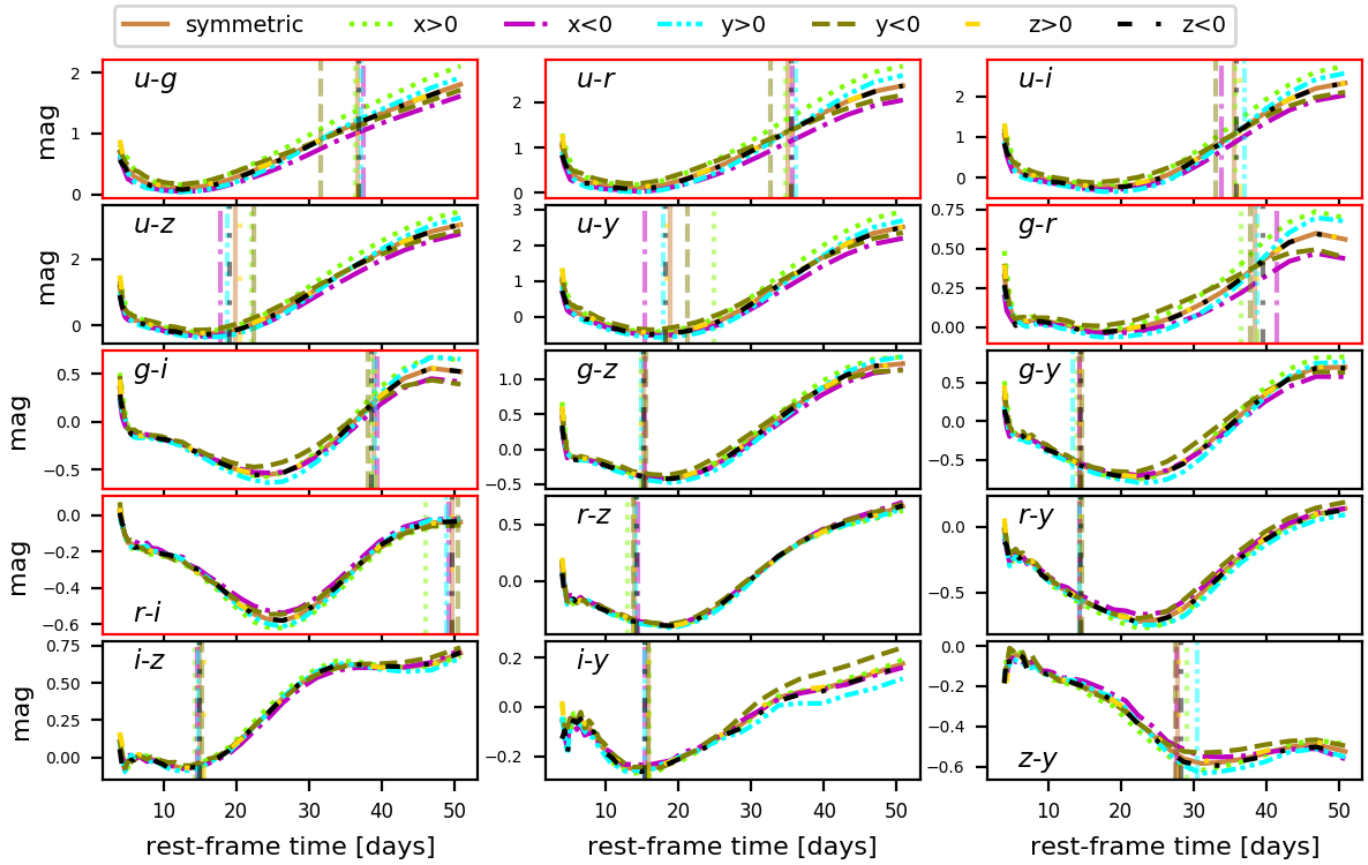

Fig. 9. All rest-frame LSST color curves without microlensing for the merger model assuming spherical symmetry and six asymmetric versions of the merger model. The vertical lines indicate the duration of the achromatic phase and red frames mark color curves that are promising for time-delay measurements. The similarities between the symmetric case and the asymmetric cases show that viewing angle effects do not influence our conclusions.

the shapes of color curves in the rest-frame UV are more uncertain. With future more detailed radiative transfer calculations, one might find useful color curves also in the rest-frame UV but chances are low since only rest-frame UV colors of the merger model show features within the achromatic phase, and all other models do not (see Appendix C).

Nevertheless these results suggest we need to follow up more in the infrared regime that corresponds to the promising rest-frame color curves shown in Fig. 6, especially for $z_s \gtrsim 0.6$. Apparent magnitudes for the six LSST filters as well as three infrared bands (J, H, and K) are shown in Fig. 11. From this we find that in the u and K bands the light curves are too faint but follow-up in all other bands seems reasonable. Huber et al. (2019) have investigated light curves for time-delay measurement and found that the combination of g, r, and i performs a few percent better than r, i, and z. The reason for this is the assumed LSST-like 5σ depth, which is nearly two magnitudes shallower in the z band in comparison to the g band (in single visits). In the context of this work, *riz* might be chosen over *gri* for having more useful color curves. Nevertheless, three bands are not ideal since this would result in just two independent color curves. The more filters used for follow-up, the higher the chances are to get promising color curves. A set of six filters with r, i, z, y, J, and H seems most promising as this would include all useful rest-frame LSST color curves shown in Fig. 6 for typical source redshifts. If resources for a further band are available, then also the g band can be used. Covering this range of bands with a single follow-up telescope might be challenging. If only an optical or only an infrared facility is available, then we recommend to observe in the redder parts of the optical coverage (*rizy* bands) since these bands would yield better quality light curves given that LSNe Ia are bright there and observational uncertainties are lower than in the infrared regime. Only for high redshift cases ($z_s \gtrsim 0.9$) it would be worth to prefer the near-infrared over the optical range.

5. Discussion and summary

According to Goldstein et al. (2018), the achromatic phase lasts for three rest-frame weeks for the W7 model (Nomoto et al. 1984), which means that in this time frame, color curves are nearly independent of microlensing and therefore promising for time-delay measurements. In this work, we investigate in addition to the W7 model, a sub-Ch model (Sim et al. 2010), a merger model (Pakmor et al. 2012), and a 3D delayed detonation model (model N100 of Seitenzahl et al. 2013). Our results are in good agreement with Goldstein et al. (2018) leading on average to an achromatic phase around three rest-frame weeks or longer. Furthermore, we do not find a significant model dependency and also asymmetries in the merger model do not have a strong influence on the duration of the achromatic phase. While this sounds very promising for time-delay measurements, there are also downsides to report. From the 15 rest-frame LSST color curves, only six show promising features for time-delay measurements and just three of them are independent. These color curves contain combinations of the rest-frame filters u, g, r, and i. To observe these for typical LSN Ia redshifts, follow-up from

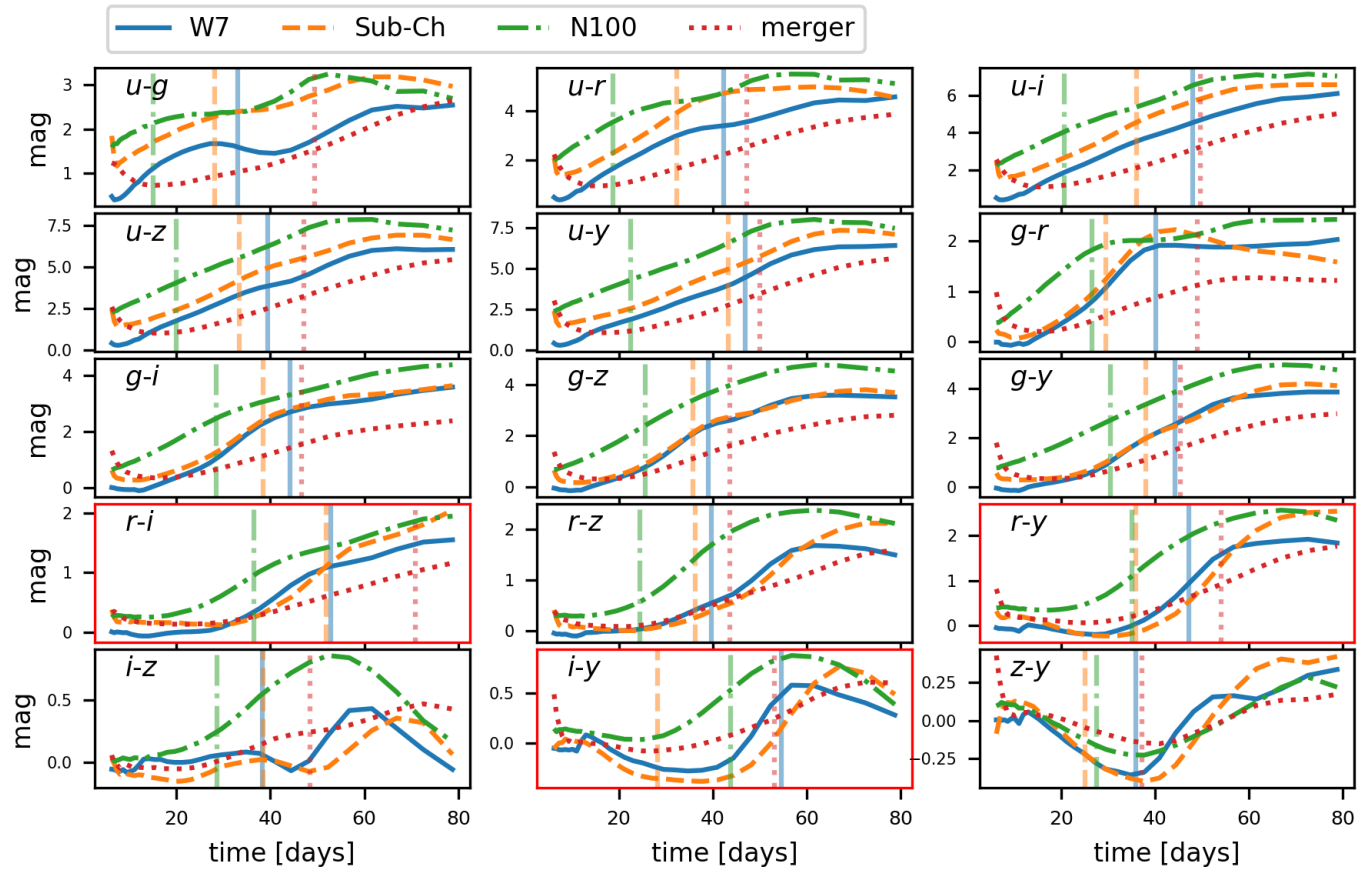

Fig. 10. All redshifted (z_s = 0.55) LSST color curves without microlensing for four different SN Ia models. The vertical lines mark the duration of the achromatic phase and red frames indicate color curves that are promising for time-delay measurements, in other words, color curves exhibiting features like extreme points or turning points that are located within the achromatic phase for at least three SNe Ia models.

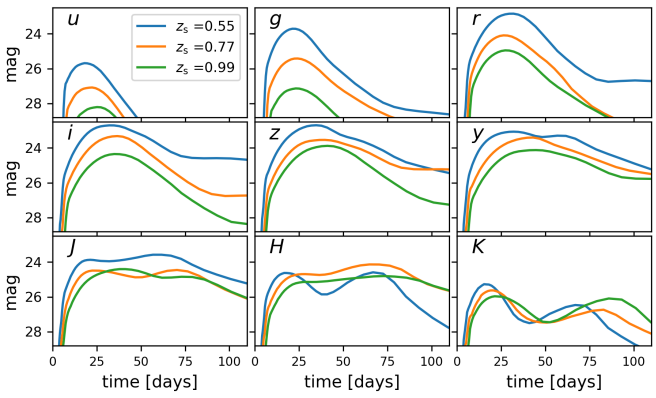

Fig. 11. Redshifted observed light curves for nine different filters and three different redshifts assuming the sub-Ch model. Light curves are too faint in the *u* and *K* bands but all other bands are potential candidates for follow-up observations.

bands *r* to *H* is necessary. In an ideal follow-up scenario, one would observe in bands *r*, *i*, *z*, *y*, *J*, *H*, and optionally also *g*. The bare minimum should cover *r*, *i*, and *z*. Observations just in three filters would make time-delay measurements from color curves hard, but in *riz* one can expect good quality light curves that can also be used for time-delay measurements (Huber et al. 2019) although microlensing uncertainties are larger.

Even though the duration of the average achromatic phase is around three rest-frame weeks or longer for most color curves, the spread of the duration is quite large. Depending on the configuration in the microlensing map, a very short achromatic phase of just a few days is also possible. Overall we find a longer achromatic phase for smoother microlensing maps (high *s* value) and image configurations with lower magnification factors. The trend that combinations of z_s, z_d, which yield a larger Einstein radius R_{Ein}, provide a longer achromatic phase is only very weak. Even though low *s* values and high magnification cases provide a shorter duration of the achromatic phase, the median for these images is still around three rest-frame weeks. Therefore, lens and image properties of a LSNe Ia (z_s, z_d, κ, γ, and *s*) can be mostly neglected when allocating follow-up observations, except z_s, which sets the filters to target.

This study provides general guidance on the observing filters to follow up LSN Ia. In a real detection of a LSNe Ia where we have the SN redshift measurement, we can further refine and optimize the filters we have to employ to get promising color curves on a case-by-case basis.

Acknowledgements. We thank M. Oguri and P. Marshall for the useful lens catalog from Oguri & Marshall (2010), and W. Hillebrandt, S. Blondin, D. A. Goldstein for useful discussions. We also would like to thank the anonymous referee for helpful comments, which strengthened this work. SH and SHS thank the Max Planck Society for support through the Max Planck Research Group for SHS. This project has received funding from the European Research Council (ERC) under the European Union's Horizon 2020 research and innovation programme (LENSNOVA: grant agreement No 771776; COSMICLENS: grant agreement No 787886). This research is supported in part by the Excellence Cluster ORIGINS which is funded by the Deutsche Forschungsgemeinschaft (DFG, German Research Foundation) under Germany's Excellence Strategy

– EXC-2094 – 390783311. UMN has been supported by the Transregional Collaborative Research Center TRR33 'The Dark Universe' of the Deutsche Forschungsgemeinschaft. JHHC acknowledges support from the Swiss National Science Foundation and through European Research Council (ERC) under the European Union's Horizon 2020 research and innovation programme (COSMICLENS: grant agreement No 787866). MK acknowledges support from the Klaus Tschira Foundation.

References

Barnabè, M., Czoske, O., Koopmans, L. V. E., Treu, T., & Bolton, A. S. 2011, MNRAS, 415, 2215
Baron, E., Bongard, S., Branch, D., & Hauschildt, P. H. 2006, ApJ, 645, 480
Bessell, M., & Murphy, S. 2012, PASP, 124, 140
Birrer, S., Treu, T., Rusu, C. E., et al. 2019, MNRAS, 484, 4726
Birrer, S., Shajib, A. J., Galan, A., et al. 2020, A&A, 643, A165
Bonvin, V., Chan, J. H. H., Millon, M., et al. 2018, A&A, 616, A183
Bonvin, V., Tihhonova, O., Millon, M., et al. 2019, A&A, 629, A97
Chang, K., & Refsdal, S. 1979, Nature, 282, 561
Chen, G. C.-F., Chan, J. H. H., Bonvin, V., et al. 2018, MNRAS, 481, 1115
Chen, G. C.-F., Fassnacht, C. D., Suyu, S. H., et al. 2019, MNRAS, 490, 1743
Courbin, F., Bonvin, V., Buckley-Geer, E., et al. 2018, A&A, 609, A71
Dessart, L., Hillier, D. J., Blondin, S., & Khokhlov, A. 2014, MNRAS, 441, 3249
Eliasdottir, A., Hjorth, J., Toft, S., Burud, I., & Paraficz, D. 2006, ApJS, 166, 443
Falco, E. E., Gorenstein, M. V., & Shapiro, I. I. 1985, ApJ, 289, L1
Foxley-Marrable, M., Collett, T. E., Vernardos, G., Goldstein, D. A., & Bacon, D. 2018, MNRAS, 478, 5081
Freedman, W. L., Madore, B. F., Hatt, D., et al. 2019, ApJ, 882, 34
Freedman, W. L., Madore, B. F., Hoyt, T., et al. 2020, ApJ, 891, 57
Gall, E. E. E., Taubenberger, S., Kromer, M., et al. 2012, MNRAS, 427, 994
Goldstein, D. A., & Nugent, P. E. 2017, ApJ, 834, L5
Goldstein, D. A., Nugent, P. E., Kasen, D. N., & Collett, T. E. 2018, ApJ, 855, 22
Goobar, A., Amanullah, R., Kulkarni, S. R., et al. 2017, Science, 356, 291
Hillebrandt, W., & Niemeyer, J. C. 2000, ARA&A, 38, 191
Hillebrandt, W., Kromer, M., Röpke, F. K., & Ruiter, A. J. 2013, Front. Phys., 8, 116
Hoyle, F., & Fowler, W. A. 1960, ApJ, 132, 565
Huber, S., Suyu, S. H., Noebauer, U. M., et al. 2019, A&A, 631, A161
Irwin, M. J., Webster, R. L., Hewett, P. C., Corrigan, R. T., & Jedrzejewski, R. I. 1989, AJ, 98, 1989
Jeffery, D. J., Leibundgut, B., Kirshner, R. P., et al. 1992, ApJ, 397, 304
Jiménez-Vicente, J., Mediavilla, E., Kochanek, C. S., & Muñoz, J. A. 2015, ApJ, 799, 149
Kasen, D., Thomas, R. C., & Nugent, P. 2006, ApJ, 651, 366
Kayser, R., Refsdal, S., & Stabell, R. 1986, A&A, 166, 36
Kelly, P. L., Brammer, G., Selsing, J., et al. 2016a, ApJ, 819, L8
Kelly, P. L., Rodney, S. A., Treu, T., et al. 2016b, ApJ, 831, 205
Khetan, N., Izzo, L., Branchesi, M., et al. 2020, ArXiv e-prints [arXiv:2008.07754]
Kromer, M., & Sim, S. A. 2009, MNRAS, 398, 1809
Kromer, M., Fremling, C., Pakmor, R., et al. 2016, MNRAS, 459, 4428
Lentz, E. J., Baron, E., Branch, D., Hauschildt, P. H., & Nugent, P. E. 2000, ApJ, 530, 966
Livio, M., & Mazzali, P. 2018, Phys. Rep., 736, 1
LSST Science Collaboration (Abell, P. A., et al.) 2009, ArXiv e-prints [arXiv:0912.0201]
Lucy, L. B. 1999, A&A, 344, 282
Mediavilla, E., Muñoz, J. A., Garzón, F., & Mahoney, T. J. 2016, Astrophysical Applications of Gravitational Lensing (Cambridge: Cambridge University Press)
Millon, M., Galan, A., Courbin, F., et al. 2020, A&A, 639, A101
Moustakas, L., Anguita, T., Chartas, G., et al. 2019, BAAS, 51, 487
Noebauer, U. M., Kromer, M., Taubenberger, S., et al. 2017, MNRAS, 472, 2787
Nomoto, K. 1982, ApJ, 253, 798
Nomoto, K., Thielemann, F.-K., & Yokoi, K. 1984, ApJ, 286, 644
Nugent, P., Baron, E., Branch, D., Fisher, A., & Hauschildt, P. H. 1997, ApJ, 485, 812
Oguri, M., & Kawano, Y. 2003, MNRAS, 338, L25
Oguri, M., & Marshall, P. J. 2010, MNRAS, 405, 2579
Oguri, M., Rusu, C. E., & Falco, E. E. 2014, MNRAS, 439, 2494
Pakmor, R., Röpke, F., Hillebrandt, W., et al. 2010, Progenitors and Environments of Stellar Explosions, 62
Pakmor, R., Hachinger, S., Röpke, F. K., & Hillebrandt, W. 2011, A&A, 528, A117
Pakmor, R., Kromer, M., Taubenberger, S., et al. 2012, ApJ, 747, L10
Pakmor, R., Kromer, M., Taubenberger, S., & Springel, V. 2013, ApJ, 770, L8
Pierel, J. D. R., & Rodney, S. 2019, ApJ, 876, 107
Planck Collaboration I. 2020, A&A, 641, A1
Quimby, R. M., Oguri, M., More, A., et al. 2014, Science, 344, 396
Refsdal, S. 1964, MNRAS, 128, 307
Riess, A. G., Macri, L. M., Hoffmann, S. L., et al. 2016, ApJ, 826, 56
Riess, A. G., Casertano, S., Yuan, W., et al. 2018, ApJ, 861, 126
Riess, A. G., Casertano, S., Yuan, W., Macri, L. M., & Scolnic, D. 2019, ApJ, 876, 85
Rusu, C. E., Madore, B. F., Hatt, D., et al. 2019, ApJ, 882, 34
Saunders, C., Aldering, G., Antilogus, P., et al. 2018, ApJ, 869, A167
Schechter, P. L., Pooley, D., Blackburne, J. A., & Wambsganss, J. 2014, ApJ, 793, 96
Schmidt, R. W., & Wambsganss, J. 2010, Gen. Relativ. Gravit., 42, 2127
Schneider, P., & Sluse, D. 2014, A&A, 564, A103
Seitenzahl, I. R., Ciaraldi-Schoolmann, F., Röpke, F. K., et al. 2013, MNRAS, 429, 1156
Shajib, A. J., Treu, T., & Agnello, A. 2018, MNRAS, 473, 210
Shajib, A., Birrer, S., Treu, T., et al. 2020, MNRAS, 494, 6072
Sim, S. A., Röpke, F. K., Hillebrandt, W., et al. 2010, ApJ, 714, L52
Sim, S. A., Seitenzahl, I. R., Kromer, M., et al. 2013, MNRAS, 436, 333
Sluse, D., Rusu, C. E., Fassnacht, C. D., et al. 2019, MNRAS, 490, 613
Suyu, S. H., Bonvin, V., Courbin, F., et al. 2017, MNRAS, 468, 2590
Suyu, S., Huber, S., Cañameras, R., et al. 2020, A&A, 644, A162
Verde, L., Treu, T., & Riess, A. G. 2019, Nat. Astron., 3, 891
Vernardos, G., & Fluke, C. J. 2013, MNRAS, 434, 832
Vernardos, G., Fluke, C. J., Bate, N. F., Croton, D., & Vohl, D. 2015, ApJS, 217, 23
Walker, E. S., Hachinger, S., Mazzali, P. A., et al. 2012, MNRAS, 427, 103
Wambsganss, J. 2006, 33rd Advanced Saas Fee Course on Gravitational Lensing: Strong, Weak, and Micro, 453
Wambsganss, J., Witt, H. J., & Schneider, P. 1992, A&A, 258, 591
Whelan, J., & Iben, I., Jr. 1973, ApJ, 186, 1007
Wojtak, R., Hjorth, J., & Gall, C. 2019, MNRAS, 487, 3342
Wong, K. C., Suyu, S. H., Chen, G. C.-F., et al. 2019, MNRAS, 498, 1420
Yahalomi, D. A., Schechter, P. L., & Wambsganss, J. 2017, ArXiv e-prints [arXiv:1711.07919]
Yıldırım, A., van den Bosch, R. C. E., van de Ven, G., et al. 2017, MNRAS, 468, 4216
Yıldırım, A., Suyu, S. H., & Halkola, A. 2020, MNRAS, 493, 4783

Appendix A: Microlensing maps

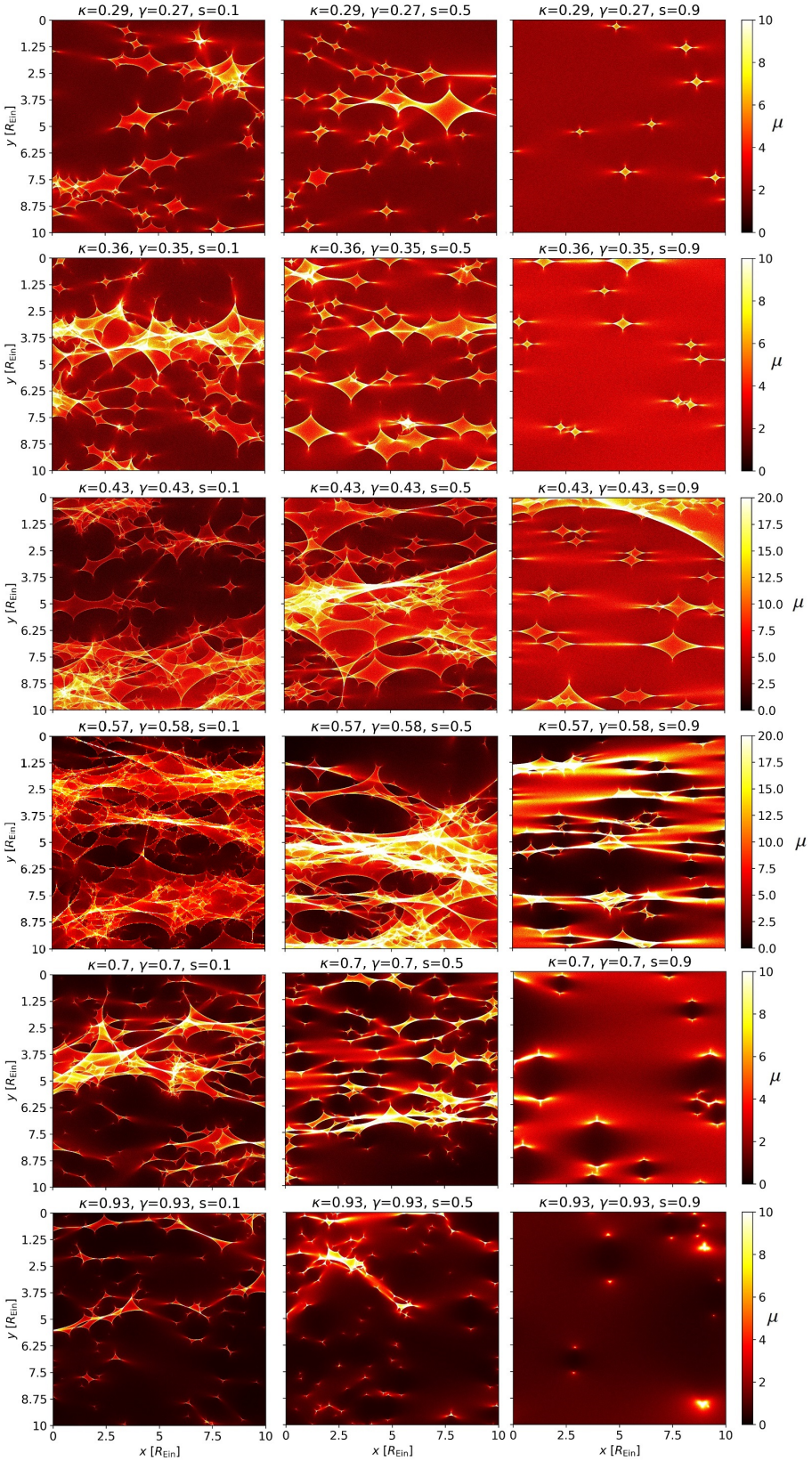

Fig. A.1. Magnification maps for six different κ and γ values with smooth matter fraction s = 0.1, 0.5, and 0.9.

Appendix B: Achromatic phase in detail

Table B.1. Duration of the achromatic phase t_{achro} in rest-frame days for all 15 LSST color curves for the W7 and N100 model and 30 different microlensing magnification maps (κ, γ, and s) as in Sect. 4.1, where for each map 10 000 random positions are drawn.

	κ, γ	s	$u-g$	$u-r$	$u-i$	$u-z$	$u-y$	$g-r$	$g-i$	$g-z$	$g-y$	$r-i$	$r-z$	$r-y$	$i-z$	$i-y$	$z-y$
W7	0.36, 0.35	0.1	39.8	31.1	28.7	19.0	19.0	31.1	24.3	16.2	16.2	31.1	16.2	14.9	17.5	17.5	31.1
		0.3	36.6	31.1	28.7	19.0	17.5	26.4	24.3	14.9	14.9	31.1	14.9	13.7	17.5	17.5	31.1
		0.5	36.6	31.1	26.4	17.5	17.5	26.4	24.3	14.9	14.9	28.7	14.9	13.7	17.5	16.2	31.1
		0.7	39.8	31.1	31.1	36.6	33.8	31.1	24.3	17.5	19.0	50.8	17.5	16.2	19.0	19.0	33.8
		0.9	50.8	39.8	39.8	46.8	39.8	36.6	36.6	50.8	39.8	50.8	43.2	50.8	43.2	50.8	43.2
	0.29, 0.27	0.1	39.8	31.1	28.7	33.8	31.1	31.1	24.3	16.2	17.5	31.1	16.2	14.9	19.0	17.5	31.1
		0.3	39.8	31.1	28.7	33.8	31.1	31.1	24.3	16.2	17.5	46.8	16.2	16.2	17.5	17.5	33.8
		0.5	39.8	31.1	28.7	19.0	19.0	31.1	24.3	16.2	16.2	31.1	16.2	14.9	17.5	17.5	31.1
		0.7	46.8	33.8	33.8	39.8	36.6	33.8	31.1	39.8	36.6	50.8	43.2	22.4	24.3	22.4	39.8
		0.9	50.8	50.8	50.8	50.8	50.8	50.8	50.8	50.8	50.8	50.8	50.8	50.8	50.8	50.8	50.8
	0.43, 0.43	0.1	39.8	31.1	28.7	19.0	19.0	31.1	24.3	16.2	16.2	31.1	16.2	14.9	17.5	17.5	31.1
		0.3	39.8	31.1	28.7	17.5	17.5	26.4	24.3	14.9	14.9	31.1	14.9	4.0	17.5	17.5	31.1
		0.5	36.6	31.1	26.4	17.5	17.5	26.4	24.3	14.9	14.9	28.7	14.9	13.7	17.5	16.2	31.1
		0.7	33.8	28.7	26.4	17.5	16.2	26.4	24.3	14.9	13.7	28.7	14.9	4.0	17.5	16.2	31.1
		0.9	39.8	31.1	31.1	33.8	33.8	31.1	24.3	16.2	17.5	50.8	16.2	16.2	19.0	17.5	33.8
	0.70, 0.70	0.1	33.8	26.4	24.3	16.2	14.9	24.3	22.4	13.7	13.7	24.3	13.7	4.0	16.2	13.7	28.7
		0.3	33.8	26.4	24.3	16.2	16.2	24.3	22.4	14.9	13.7	26.4	14.9	13.7	17.5	14.9	28.7
		0.5	31.1	26.4	24.3	14.9	13.7	24.3	22.4	12.6	11.6	17.5	12.6	4.0	16.2	13.7	22.4
		0.7	33.8	31.1	28.7	33.8	31.1	28.7	24.3	17.5	17.5	28.7	17.5	16.2	19.0	19.0	31.1
		0.9	50.8	39.8	43.2	46.8	43.2	39.8	39.8	50.8	43.2	50.8	43.2	50.8	43.2	50.8	43.2
	0.57, 0.58	0.1	36.6	28.7	26.4	17.5	17.5	26.4	24.3	14.9	14.9	28.7	14.9	4.0	17.5	16.2	31.1
		0.3	36.6	31.1	26.4	17.5	17.5	26.4	24.3	14.9	14.9	28.7	14.9	4.0	17.5	16.2	31.1
		0.5	33.8	26.4	24.3	16.2	16.2	24.3	22.4	13.7	13.7	24.3	13.7	4.0	16.2	14.9	28.7
		0.7	31.1	26.4	24.3	14.9	14.9	24.3	22.4	12.6	4.0	24.3	4.0	4.0	16.2	13.7	20.7
		0.9	31.1	26.4	24.3	14.9	13.7	22.4	22.4	12.6	11.6	16.2	12.6	5.6	16.2	13.7	20.7
	0.93, 0.93	0.1	33.8	28.7	26.4	19.0	17.5	26.4	24.3	16.2	16.2	28.7	16.2	14.9	17.5	17.5	31.1
		0.3	33.8	28.7	26.4	19.0	17.5	26.4	24.3	16.2	16.2	28.7	16.2	14.9	17.5	17.5	31.1
		0.5	43.2	33.8	31.1	36.6	33.8	33.8	28.7	20.7	33.8	50.8	19.0	19.0	20.7	20.7	36.6
		0.7	50.8	39.8	39.8	46.8	39.8	36.6	36.6	50.8	39.8	50.8	43.2	50.8	43.2	50.8	43.2
		0.9	50.8	50.8	50.8	50.8	50.8	50.8	50.8	50.8	50.8	50.8	50.8	50.8	50.8	50.8	50.8
	Mean		**39.2**	**32.2**	**30.4**	**26.8**	**25.3**	**30.3**	**27.4**	**22.1**	**21.2**	**35.1**	**21.1**	**18.1**	**22.6**	**22.5**	**33.1**
N100	0.36, 0.35	0.1	20.7	17.5	14.9	31.1	17.5	19.0	12.6	17.5	19.0	26.4	13.7	4.0	9.1	43.2	14.9
		0.3	19.0	17.5	14.9	31.1	17.5	19.0	12.6	17.5	19.0	26.4	13.7	4.0	9.1	43.2	14.9
		0.5	19.0	16.2	14.9	31.1	17.5	19.0	13.7	16.2	19.0	26.4	13.7	26.4	9.1	43.2	14.9
		0.7	20.7	19.0	16.2	31.1	19.0	20.7	16.2	19.0	28.7	50.8	14.9	43.2	12.6	43.2	16.2
		0.9	43.2	31.1	33.8	50.8	33.8	39.8	39.8	50.8	36.6	50.8	24.3	50.8	43.2	50.8	39.8
	0.29, 0.27	0.1	20.7	17.5	16.2	31.1	19.0	20.7	14.9	17.5	20.7	26.4	14.9	43.2	9.9	43.2	14.9
		0.3	20.7	17.5	16.2	31.1	19.0	20.7	16.2	19.0	26.4	28.7	14.9	43.2	11.6	43.2	16.2
		0.5	20.7	17.5	14.9	31.1	19.0	19.0	14.9	17.5	20.7	26.4	13.7	43.2	10.7	43.2	14.9
		0.7	31.1	26.4	28.7	36.6	31.1	33.8	36.6	43.2	36.6	50.8	20.7	46.8	20.7	50.8	20.7
		0.9	50.8	46.8	46.8	43.2	46.8	50.8	50.8	50.8	50.8	50.8	50.8	50.8	50.8	50.8	46.8
	0.43, 0.43	0.1	20.7	17.5	14.9	31.1	19.0	19.0	13.7	17.5	20.7	26.4	4.0	4.0	9.1	43.2	14.9
		0.3	19.0	17.5	13.7	31.1	17.5	19.0	12.6	17.5	19.0	26.4	4.0	4.0	5.1	43.2	14.9
		0.5	19.0	16.2	13.7	31.1	17.5	17.5	11.6	16.2	19.0	26.4	4.0	4.0	7.1	9.1	13.7
		0.7	17.5	16.2	12.6	31.1	16.2	17.5	11.6	4.0	4.0	26.4	4.0	4.0	4.0	4.0	13.7
		0.9	22.4	19.0	17.5	31.1	20.7	22.4	16.2	19.0	28.7	50.8	14.9	43.2	11.6	43.2	16.2
	0.70, 0.70	0.1	14.9	13.7	10.7	28.7	14.9	16.2	10.7	4.0	4.0	13.7	4.0	4.0	4.0	4.0	12.6
		0.3	14.9	13.7	11.6	26.4	14.9	16.2	11.6	13.7	17.5	13.7	5.1	24.3	7.1	7.7	12.6
		0.5	13.7	12.6	10.7	24.3	14.9	16.2	10.7	4.0	4.0	12.6	4.0	4.0	4.0	4.0	12.6
		0.7	19.0	17.5	14.9	28.7	17.5	19.0	16.2	17.5	20.7	26.4	14.9	43.2	11.6	43.2	14.9
		0.9	36.6	31.1	33.8	43.2	33.8	39.8	39.8	50.8	39.8	50.8	39.8	50.8	39.8	50.8	39.8
	0.57, 0.58	0.1	17.5	16.2	12.6	28.7	16.2	17.5	11.6	16.2	17.5	24.3	4.0	4.0	5.1	7.7	13.7
		0.3	19.0	16.2	12.6	31.1	17.5	17.5	11.6	16.2	17.5	26.4	4.0	4.0	5.1	9.1	13.7
		0.5	16.2	14.9	11.6	28.7	14.9	16.2	10.7	4.0	4.0	24.3	4.0	4.0	4.0	4.0	12.6
		0.7	14.9	12.6	9.9	26.4	14.9	16.2	9.9	4.0	4.0	12.6	4.0	4.0	4.0	4.0	12.6
		0.9	13.7	12.6	9.9	20.7	13.7	14.9	10.7	5.1	4.0	11.6	4.0	4.0	4.0	4.0	12.6
	0.93, 0.93	0.1	19.0	16.2	13.7	28.7	17.5	19.0	13.7	16.2	19.0	26.4	13.7	26.4	9.9	43.2	14.9
		0.3	17.5	16.2	13.7	28.7	16.2	19.0	13.7	16.2	19.0	24.3	13.7	26.4	9.9	39.8	14.9
		0.5	22.4	20.7	20.7	31.1	22.4	24.3	31.1	20.7	31.1	50.8	17.5	43.2	14.9	43.2	17.5
		0.7	31.1	26.4	28.7	36.6	31.1	36.6	36.6	50.8	36.6	50.8	24.3	50.8	36.6	50.8	24.3
		0.9	50.8	50.8	50.8	50.8	50.8	50.8	50.8	50.8	50.8	50.8	50.8	50.8	50.8	50.8	50.8
	Mean		**22.9**	**20.2**	**18.5**	**32.2**	**21.4**	**23.2**	**19.5**	**21.1**	**22.0**	**31.3**	**14.5**	**25.3**	**14.5**	**32.1**	**18.9**

Notes. The mean values are plotted in Fig. 6.

Table B.2. Duration of the achromatic phase $t_{\rm achro}$ in rest-frame days for all 15 LSST color curves for the sub-Ch and the merger model and 30 different microlensing magnification maps (κ, γ, and s) as in Sect. 4.1, where for each map 10 000 random positions are drawn.

	κ, γ	s	$u-g$	$u-r$	$u-i$	$u-z$	$u-y$	$g-r$	$g-i$	$g-z$	$g-y$	$r-i$	$r-z$	$r-y$	$i-z$	$i-y$	$z-y$
Sub-Ch	0.36, 0.35	0.1	31.1	31.1	31.1	17.5	14.9	36.6	36.6	12.6	10.7	50.8	14.9	6.0	14.9	6.6	26.4
		0.3	31.1	28.7	31.1	16.2	13.7	36.6	36.6	11.6	9.9	50.8	14.9	6.0	14.9	6.0	24.3
		0.5	28.7	28.7	28.7	16.2	12.6	36.6	33.8	11.6	9.9	50.8	14.9	6.6	14.9	6.6	24.3
		0.7	31.1	31.1	31.1	36.6	31.1	36.6	36.6	14.9	13.7	50.8	16.2	14.9	17.5	12.6	26.4
		0.9	46.8	39.8	43.2	50.8	43.2	46.8	46.8	50.8	46.8	50.8	46.8	50.8	46.8	50.8	46.8
	0.29, 0.27	0.1	31.1	31.1	31.1	19.0	17.5	36.6	36.6	12.6	11.6	50.8	16.2	7.7	16.2	7.7	26.4
		0.3	31.1	31.1	31.1	36.6	31.1	36.6	36.6	13.7	12.6	50.8	16.2	11.6	17.5	10.7	26.4
		0.5	31.1	31.1	31.1	20.7	17.5	36.6	36.6	12.6	11.6	50.8	16.2	9.9	17.5	9.1	26.4
		0.7	33.8	33.8	36.6	43.2	36.6	43.2	43.2	50.8	43.2	50.8	43.2	50.8	39.8	50.8	39.8
		0.9	50.8	50.8	50.8	50.8	50.8	50.8	50.8	50.8	50.8	50.8	50.8	50.8	50.8	50.8	50.8
	0.43, 0.43	0.1	31.1	31.1	31.1	17.5	14.9	36.6	36.6	11.6	9.9	50.8	14.9	6.0	14.9	6.0	26.4
		0.3	31.1	31.1	31.1	16.2	12.6	36.6	36.6	11.6	9.9	50.8	4.0	5.6	6.0	6.0	24.3
		0.5	28.7	28.7	28.7	16.2	12.6	36.6	33.8	11.6	9.1	50.8	4.0	5.6	6.0	6.0	24.3
		0.7	28.7	28.7	28.7	14.9	9.9	36.6	33.8	9.1	8.4	46.8	4.0	4.4	4.0	5.6	20.7
		0.9	31.1	31.1	31.1	36.6	31.1	36.6	36.6	13.7	12.6	50.8	16.2	12.6	17.5	11.6	26.4
	0.70, 0.70	0.1	26.4	26.4	26.4	12.6	8.4	12.6	28.7	6.0	6.6	28.7	4.0	4.4	4.0	4.4	19.0
		0.3	26.4	28.7	28.7	14.9	10.7	13.7	31.1	9.9	9.1	31.1	6.0	6.0	6.6	6.0	20.7
		0.5	26.4	26.4	26.4	11.6	8.4	12.6	16.2	6.6	7.7	26.4	4.0	4.4	4.0	5.6	17.5
		0.7	28.7	28.7	28.7	33.8	31.1	36.6	36.6	14.9	14.9	46.8	17.5	14.9	17.5	14.9	26.4
		0.9	39.8	36.6	39.8	50.8	39.8	46.8	46.8	50.8	46.8	50.8	46.8	50.8	46.8	50.8	43.2
	0.57, 0.58	0.1	28.7	28.7	28.7	16.2	11.6	36.6	33.8	9.9	8.4	46.8	4.0	4.4	6.0	5.6	22.4
		0.3	28.7	28.7	28.7	16.2	11.6	36.6	33.8	11.6	9.1	46.8	4.0	5.6	6.0	6.0	24.3
		0.5	28.7	28.7	28.7	12.6	9.1	13.7	31.1	8.4	7.7	46.8	4.0	4.4	4.0	5.6	19.0
		0.7	26.4	26.4	26.4	11.6	7.7	12.6	16.2	5.6	6.0	26.4	4.0	4.4	4.0	4.4	17.5
		0.9	24.3	13.7	26.4	11.6	9.1	12.6	16.2	7.7	7.7	26.4	4.0	5.6	5.6	5.6	17.5
	0.93, 0.93	0.1	28.7	28.7	28.7	17.5	14.9	36.6	33.8	12.6	11.6	46.8	16.2	10.7	14.9	9.9	24.3
		0.3	28.7	28.7	28.7	16.2	13.7	36.6	33.8	11.6	9.9	46.8	14.9	7.7	14.9	7.7	24.3
		0.5	31.1	31.1	33.8	36.6	33.8	39.8	39.8	19.0	39.8	50.8	20.7	19.0	20.7	19.0	31.1
		0.7	36.6	36.6	36.6	46.8	36.6	43.2	43.2	50.8	43.2	50.8	43.2	50.8	43.2	50.8	39.8
		0.9	50.8	50.8	50.8	50.8	50.8	50.8	50.8	50.8	50.8	50.8	50.8	50.8	50.8	50.8	50.8
	Mean		**31.9**	**31.2**	**32.1**	**25.6**	**21.6**	**34.1**	**35.4**	**19.2**	**18.3**	**46.1**	**17.9**	**16.4**	**18.3**	**16.5**	**27.9**
Merger	0.36, 0.35	0.1	43.2	36.6	36.6	5.1	4.0	39.8	39.8	4.0	4.0	50.8	4.0	4.0	5.6	4.7	24.3
		0.3	43.2	36.6	36.6	17.5	4.7	39.8	39.8	4.0	4.0	50.8	4.4	4.0	5.6	4.7	24.3
		0.5	39.8	33.8	33.8	14.9	4.7	36.6	36.6	4.7	4.7	50.8	4.7	4.7	5.6	4.7	24.3
		0.7	43.2	36.6	39.8	22.4	43.2	39.8	39.8	13.7	8.4	50.8	14.9	8.4	17.5	17.5	28.7
		0.9	50.8	46.8	46.8	50.8	50.8	50.8	50.8	50.8	50.8	50.8	43.2	50.8	43.2	50.8	43.2
	0.29, 0.27	0.1	43.2	36.6	36.6	17.5	8.4	39.8	39.8	5.1	4.7	50.8	5.1	4.7	13.7	5.6	28.7
		0.3	43.2	36.6	36.6	19.0	43.2	39.8	39.8	6.0	5.6	50.8	6.0	5.6	14.9	7.7	28.7
		0.5	43.2	36.6	36.6	19.0	14.9	39.8	39.8	6.0	5.6	50.8	6.0	5.6	13.7	8.4	24.3
		0.7	50.8	43.2	43.2	28.7	46.8	46.8	43.2	24.3	46.8	50.8	22.4	50.8	24.3	50.8	39.8
		0.9	50.8	50.8	50.8	50.8	50.8	50.8	50.8	50.8	50.8	50.8	50.8	50.8	50.8	50.8	50.8
	0.43, 0.43	0.1	43.2	39.8	39.8	4.4	4.0	39.8	39.8	4.0	4.0	50.8	4.0	4.0	4.7	4.7	28.7
		0.3	43.2	36.6	36.6	4.0	4.0	39.8	39.8	4.0	4.0	50.8	4.0	4.0	4.7	4.7	24.3
		0.5	43.2	36.6	36.6	4.4	4.0	39.8	36.6	4.0	4.0	50.8	4.0	4.0	4.7	4.7	24.3
		0.7	39.8	33.8	33.8	4.0	4.0	36.6	36.6	4.0	4.0	50.8	4.0	4.0	4.7	4.0	24.3
		0.9	46.8	39.8	39.8	22.4	43.2	43.2	39.8	13.7	9.9	50.8	14.9	9.1	17.5	19.0	33.8
	0.70, 0.70	0.1	22.4	28.7	28.7	4.0	4.0	31.1	33.8	4.0	4.0	46.8	4.0	4.0	4.7	4.0	22.4
		0.3	22.4	28.7	28.7	10.7	5.1	31.1	33.8	4.7	4.7	46.8	5.1	4.7	5.6	4.7	22.4
		0.5	20.7	22.4	24.3	4.4	4.0	28.7	31.1	4.0	4.0	46.8	4.0	4.0	4.7	4.7	20.7
		0.7	31.1	33.8	33.8	19.0	20.7	36.6	36.6	11.6	8.4	50.8	11.6	8.4	14.9	11.6	24.3
		0.9	50.8	46.8	46.8	50.8	46.8	50.8	46.8	50.8	50.8	50.8	43.2	50.8	43.2	50.8	43.2
	0.57, 0.58	0.1	36.6	33.8	33.8	4.0	4.0	36.6	36.6	4.0	4.0	50.8	4.0	4.0	4.7	4.0	24.3
		0.3	39.8	33.8	33.8	4.0	4.0	39.8	36.6	4.0	4.0	50.8	4.0	4.0	4.7	4.7	24.3
		0.5	24.3	31.1	31.1	4.0	4.0	33.8	33.8	4.0	4.0	50.8	4.0	4.0	4.7	4.0	22.4
		0.7	20.7	24.3	26.4	4.0	4.0	28.7	33.8	4.0	4.0	46.8	4.0	4.0	4.7	4.0	20.7
		0.9	19.0	20.7	20.7	4.4	4.0	26.4	31.1	4.0	4.0	43.2	4.0	4.0	4.7	4.7	20.7
	0.93, 0.93	0.1	31.1	33.8	33.8	17.5	13.7	36.6	36.6	7.7	7.1	50.8	7.7	6.6	13.7	8.4	24.3
		0.3	26.4	31.1	31.1	16.2	9.9	33.8	36.6	6.0	5.6	50.8	6.0	5.6	12.6	7.1	22.4
		0.5	46.8	39.8	39.8	33.8	43.2	43.2	39.8	19.0	43.2	50.8	20.7	22.4	20.7	26.4	33.8
		0.7	46.8	43.2	43.2	50.8	46.8	46.8	46.8	50.8	46.8	50.8	39.8	50.8	39.8	50.8	43.2
		0.9	50.8	50.8	50.8	50.8	50.8	50.8	50.8	50.8	50.8	50.8	50.8	50.8	50.8	50.8	50.8
	Mean		**38.6**	**36.1**	**36.4**	**18.8**	**19.9**	**39.2**	**39.2**	**14.3**	**15.2**	**50.0**	**13.5**	**14.8**	**15.5**	**16.1**	**29.1**

Notes. The mean values are plotted in Fig. 6.

Appendix C: Additional color curves

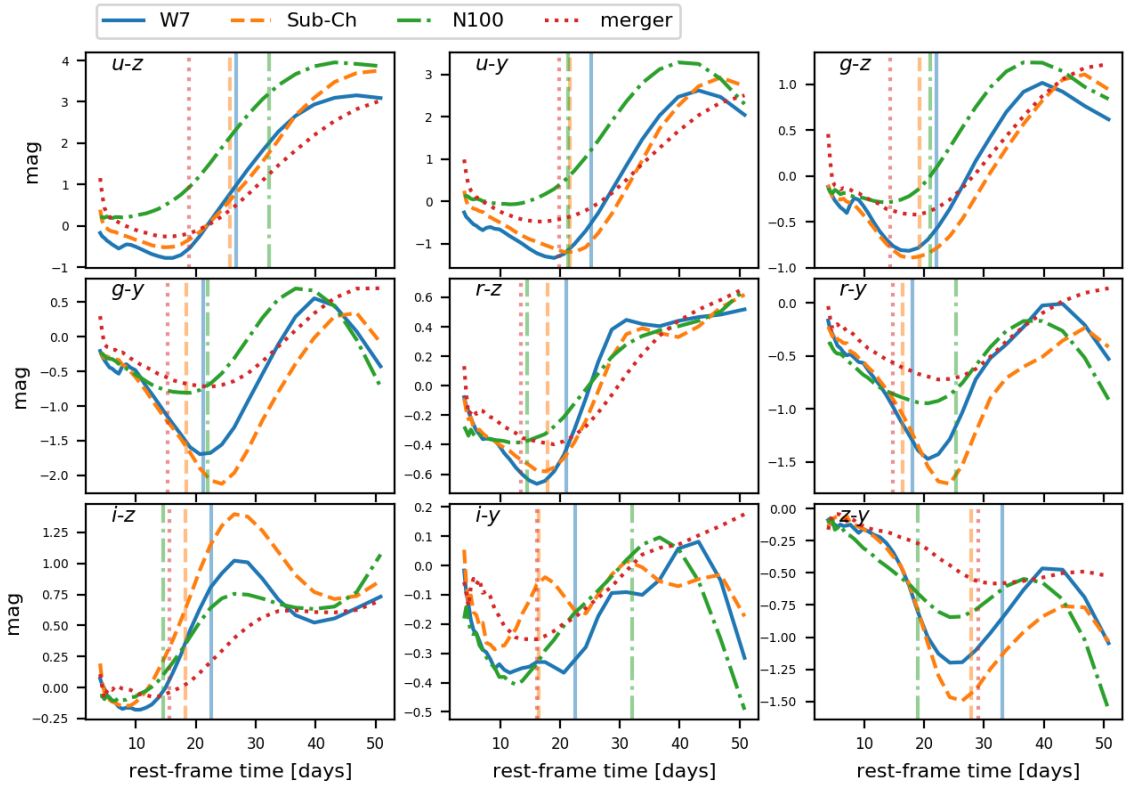

Fig. C.1. Rest-frame LSST color curves without microlensing for four different SN Ia models similar as in Fig. 6, but this time showing the remaining nine color curves that are not as useful for time-delay measurements.

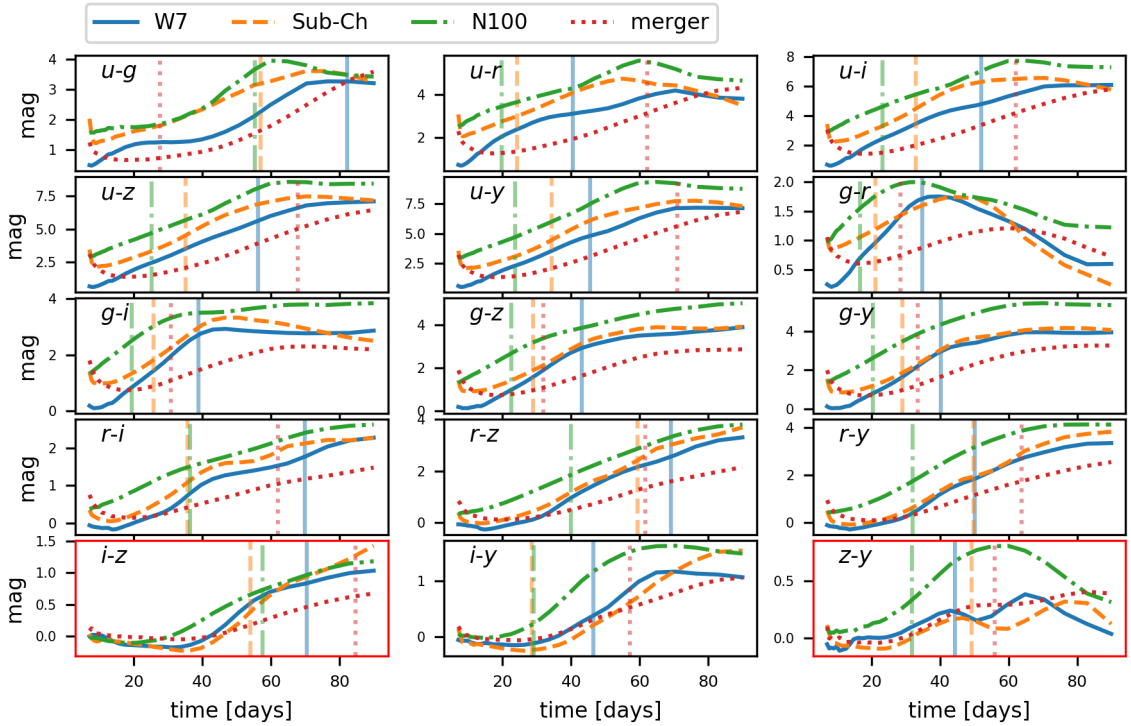

Fig. C.2. All redshifted LSST color curves without microlensing for four different SN Ia models similar to Fig. 10 but at $z_s = 0.77$.

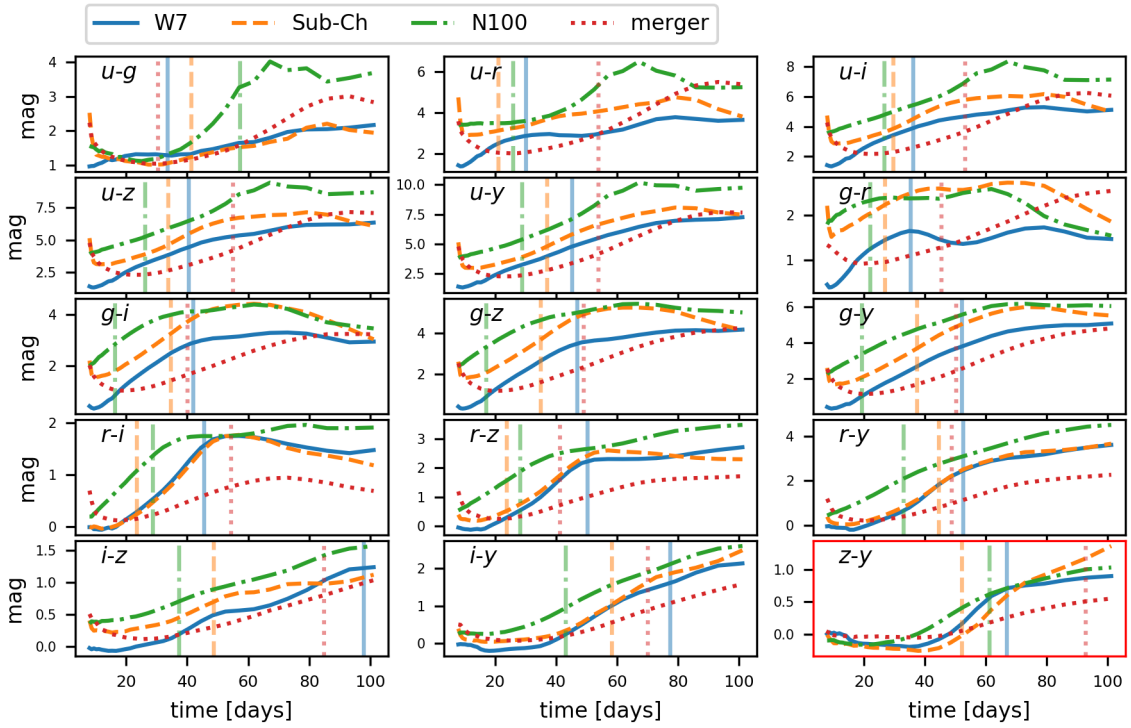

Fig. C.3. All redshifted LSST color curves without microlensing for four different SN Ia models similar to Fig. 10 but at $z_s = 0.99$.